Synthesis and Characterization of Thermoelectric Half-Heusler alloy TiFeSb

by

Kenneth Kjeverud Strand

Master Thesis

in

Materials, Energy and Nanotechnology

The Faculty of Mathematics and Natural Sciences

University of Oslo

June 1, 2014

Contents

List of Figures

List of Tables

Abstract

In recent years there has been an increased demand for more sustainable and cleaner energy sources. Thermoelectric modules have the potential as clean and environmentally friendly power sources, which generate power from the waste-heat of different industrial processes, that are otherwise lost to the surroundings.
Thermoelectric Half-Heusler alloys have received interest because of the abundance and non-toxicity of readily available elements which can compose these alloys, and their promising electrical transport properties. It is therefore much interest around finding cheap and efficient materials for large scale production.

This thesis investigated a TiFeSb alloy with emphasis on the thermoelectric properties. The system has a general formula XYZ in a 1:1:1 stoichiometry, which crystallize in Space group 216, $F\bar{4}3m$, $C1_b$. Synthesis, structural and electrical characterization have been carried out by different methods. The samples are synthesized by electric arc-melting and have undergone annealing and sintering for refinement of the structure. Electrical characterization has been done by the Laser Flash method for thermal conductivity, Van der Pauw method for resistivity and Hall measurements, and a custom set-up for determination of Seebeck-coefficients.

Thermal conductivities are found in the range of 2.5-4.5 $\mathrm{WK^{-1}m^{-1}}$, Electrical resistivities are around 1.4-2.1$\cdot 10^{-5}$ Ωm, and Seebeck-coefficients are found be around 50 $\frac{\mu V}{K}$. Measurements are done in a temperature range of 50°C to 500°C.
Both samples are confirmed to be p-type by the positive sign of the measured Hall voltage. The maximum ZT of the samples are achieved at 350°C, the highest ZT reached was around ZT = 0.03.

Foreword

This thesis is written as part of the master program in MENA (Materials, Energy and Nanotechnology) at the Department of Physics, University of Oslo. The work is done under the Structural Physics Group and the Basic and Applied ThermoElectrics (BATE) initiative, at the Research Park.

I want to thank my supervisors Terje Finstad and Øystein Prytz for all the help and meetings during the process of the thesis. A thank you to Annette E. Gunnæs and Johan Taftø for giving me an exciting material system to work on. A thank you to Magnus H. Sørby at IFE for assisting with the fabrication of the materials. A thank you to Ole Bjørn Karlsen and Andrey Kosinskiy for all the help in many different areas. A huge thank you to Kjetil Valset and Matthias Schrade for the help with the measurements. And a special thanks to Martin V. Normann who has been my office-buddy and one of my best friends during my years at UiO.
And of course, a thank you to my parents John Strand and Wenche Kjeverud, who have supported me and been interested in what I am doing, and without whom I wouldn't even be here.

Kenneth Kjeverud Strand
Oslo, May 2014

Chapter 1

Introduction and motivation for researching Thermoelectric Half-Heusler Materials

In recent years the demand and search for cleaner and renewable energy sources are becoming urgent, with increasing population growth which leads to an increased energy demand. Negative environmental effects from pollution such as CO_2 emissions and increased greenhouse gas effects caused by non-renewable energy sources, like fossil fuels, causes global warming which is going to have a huge impact on the quality of life on Earth. Thermoelectric energy and other renewable energy sources such as wind- and water-power can reduce these emissions and should be invested in for further research [1]. The main sources of energy today comes from oil, gas and coal. These sources will deplete, and the world will face a huge energy crisis. Oil and gas are expected to only last for another 30-40 years, while coal might be available for approximately 100 years according to Shafiee and Topal [2], although they do make a point of reserves not declining because of new reserves being found, which might double the depletion time of gas and coal. Thermoelectric materials, capable of converting waste heat to electric energy from the burning of these fossil fuels, have received extensive interest in recent years [3] [4] [5]. Among the best thermoelectric materials today based on Bi_2Te_3 and $Si_{(1-x)}Ge_x$

[6], Half-Heusler alloys have attracted great interest due to their appealing electrical transport properties. For thermoelectric devices, materials with high energy conversion efficiency and similar physical properties are needed. Most efforts have been concentrated on enhancing the performance of n-type Half-Heusler alloys so far, and studies on the p-type alloys remains few. Hence exploring potential p-type alloys or improving the performance of existing p-type alloys are important [7]. Zou et al. [7] investigated the alloy VFeSb and found that it is n-type, however they made substitution of V by Ti and found that it converts into p-type because of the one less valence electron of Ti compared to V. N-type TiNiSn-based compounds have been most intensively investigated, and great progress has been made for p-type TiCoSb-based compounds that posses a high potential for significant increase in ZT due to their still high thermal conductivity [8]. One can see from the table on p.34 in the Graf et al. [8] paper that p-type MCoSb materials exhibit several times larger thermal conductivity than the n-type MNiSn materials (M = Ti, Hf, Zr). Graf also references other papers she has been a part of that experimented on a $Ti_{(1-x)}Mn_xCoSb$ system. In this system a phase separation occurred during the solidification process into TiCoSb and MnCoSb phases. This separation led to a significant reduction in thermal conductivity due to boundary scattering mechanics. However, they point out that these mechanisms need to be further investigated in order to control and benefit fully from them. In MNiSn-materials, Sb turned out to be an effective dopant, in fact an increasing Sb content shifts the maximum of the Seebeck-coefficient to higher temperatures, therefore enhancing the power factor [8]. This thesis will investigate a TiFeSb alloy.

Chapter 2

Background on thermoelectricity

This chapter will give a short summary of how thermoelectricity has developed since it gained interest, and how it is used today. Here we will also look at the physical principles that play a part in the phenomena that arises, and how we can find them from measurements.

There are many practical uses for thermoelectricity where power supply is limited, and the systems go from being relatively basic to complex engineering. There are no moving parts in a thermoelectric module, they run silently and are without the need of maintenance over large periods of time.

2.1 History of Thermoelectric Materials

The technology of thermoelectricity began in the Soviet Union, where A.F. Ioffe produced thermoelectric generators that could power a small radio by using the heat from a cooking fire [9]. During the 1950s and 1960s there where significant efforts to further developing thermoelectric technology with advances in semiconductor technology, more efficient semiconducting alloys and advances in theory along with the enthusiasm around this new field. Most effort was done in the Soviet Union and USA, and to some extent Europe and

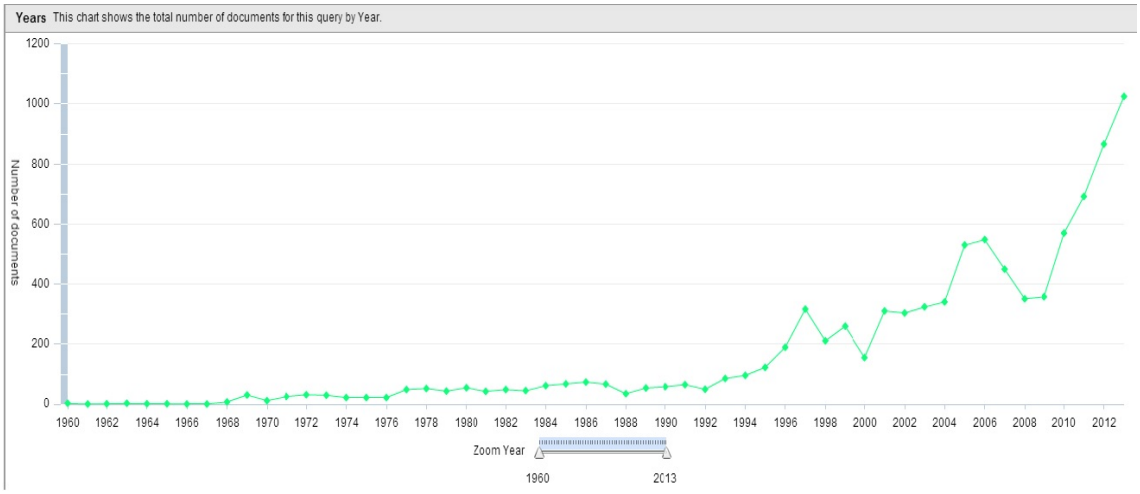

Figure 2.1: A keyword search for thermoelectricity and thermoelectrics gives a kind of measure for the interest in thermoelectricity from 1960-2013. Done at www.scopus.com for Elsevier, the site searches for published documents containing the keywords.

Japan. In the 1960s most practical thermoelectric devices where made for cooling applications in aerospace and space power generation. From there on it would take almost 30 years before the interest started rising again (Figure (2.1)), and it is rising steeper than ever. NASA found a way to use a nuclear heat source at the end of the 1960s which they called radioisotope thermoelectric generators (RTGs). These provided them with sustainable long-life power sources for use in inaccessible and hostile environments like their mission to the moon and the Voyager I and II missions. The same technology where used in medical sciences as well, the most successful being the nuclear-power thermoelectric pacemaker battery. Despite the success of the RTG, further research declined. The oil crisis of the 1970s also created a problem with funding. Even though, in 1970, Raymond Marlow and Dr. K.R. Rao teamed up to organize a series of short courses and conferences which would eventually lead to the formation of the ITC, International Thermoelectric Society. ITC started out with more speakers than attendants, but is today healthy and growing, something that can be seen from the significant increase in published work on this side of the millenium. More history can be found in the Appendix of the book edited by Rowe [9].

2.2 Physical principles

2.2.1 Seebeck Effect

Thomas Seebeck discovered that two different conductors which are connected as a circuit, and subjected to a thermal gradient, will generate a voltage. This is shown in figure(2.2). It can be considered as a circuit formed from two dissimilar conductors, a and b, which are connected electrically in series, but thermally in parallel. If the junctions at A and B are maintained at different temperatures T_1 and T_2 with $T_1 > T_2$ an open circuit electromotive force (emf), or voltage V, is developed between C and D and given by

$$V = \alpha_{ab}(T_1 - T_2) \tag{2.1}$$

or

$$\alpha_{ab} = \frac{V}{\Delta T} \tag{2.2}$$

Where V is the voltage and ΔT is the temperature difference,
which defines the differential Seebeck-coefficient α_{ab} between the elements a and b. Although α by convention is the symbol for the Seebeck-coefficient, S is sometimes used and the coefficient might be referred to as the thermal emf or thermopower. The sign of α is positive if the generated voltage causes a current to flow in a clockwise direction around the circuit and is measured in $\frac{V}{K}$, or more often in $\frac{\mu V}{K}$ [9].

2.2.2 Peltier Effect

The Peltier effect can be seen as the opposite of the Seebeck effect. It is a reverse situation where an external voltage source is applied across C and D and a current I flows in a clockwise direction around the circuit, then a rate of heating q occurs at junction A and a rate of cooling $-q$ occurs at junction B, see Figure (2.3) The ratio of I and q defines the Peltier-coefficient given by

$$\pi_{ab} = \frac{I}{q} \tag{2.3}$$

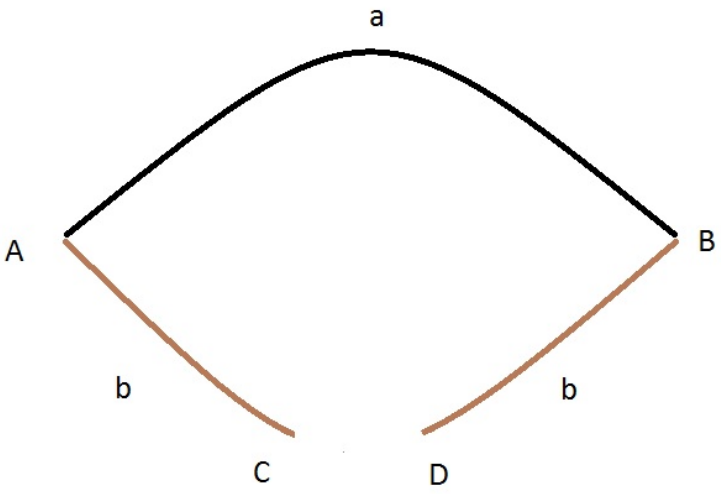

Figure 2.2: Schematic of a basic thermocouple for the Seebeck effect

Where I is the current and q is the heat.
This coefficient is positive if A is heated and B is cooled, and is measured in volts [9].

2.2.3 Thomson Effect

The last of the thermoelectric effects, the Thomson effect relates to the rate of generation of reversible heat q which results from passing a current along a single conductor which is subjected to a thermal gradient ΔT. The effect might show itself as heat absorbation or heat release in different conductors. The Thomson-coefficient is given by

$$q = \beta I \Delta T \tag{2.4}$$

Where q is the heat, β is the Thomson-coefficient, and ΔT is the temperature difference.
The units of β is the same as those of the Seebeck-coefficient $\frac{V}{K}$. The Thomson effect is not of primary importance in thermoelectric devices, but should

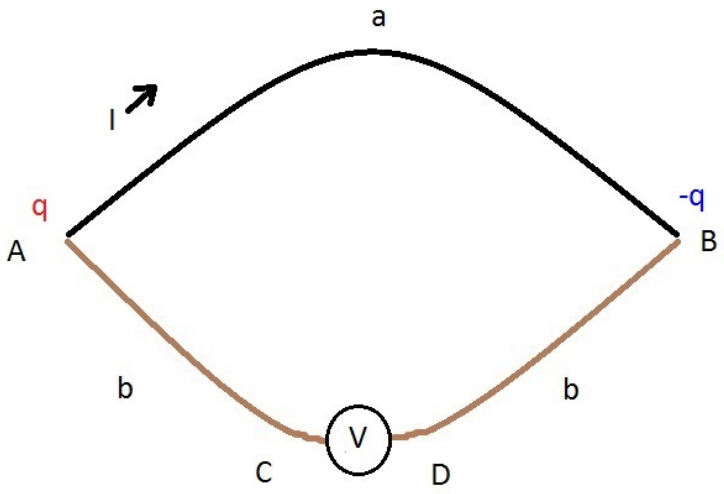

Figure 2.3: Schematic for the Peltier effect

not be neglected in detailed calculations [9].

2.2.4 The Kelvin Relationships

The above three thermoelectric coefficients are related by the Kelvin Relationships

$$\frac{d\alpha_{ab}}{dT} = \frac{\beta_a - \beta_b}{T} \tag{2.5}$$

and

$$\alpha_{ab} = \pi_{ab}/T \tag{2.6}$$

These relationships can be derived using irreversible thermodynamics. Their validity has been demonstrated for many thermoelectric materials and it is assumed that they hold for all materials used in thermoelectric applications [9].

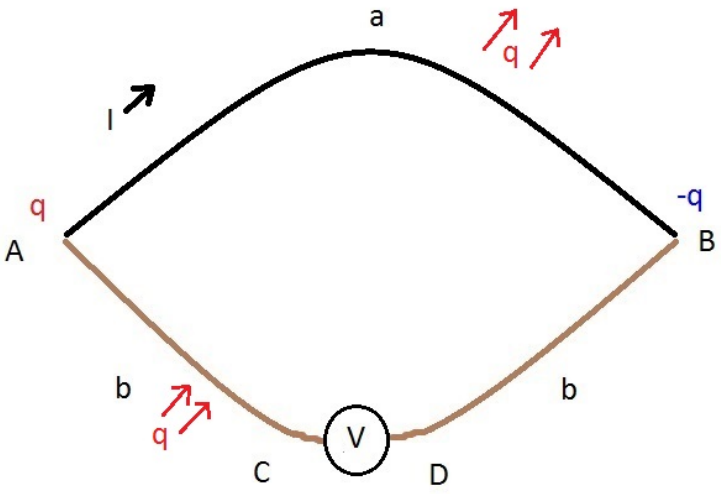

Figure 2.4: Schematic for the Thomson effect

2.3 The Figure-of-Merit

The efficiency of a thermoelectric material is the same as for a heat engine since they work the same way. Heat is brought into the system and power is the output. The efficiency is then how much electrical power is generated from the heat input. An ideal generator without any heat loss follows the theoretical Carnot efficiency

$$\eta_C = \frac{E_{out}}{Q_{in}} = \frac{T_H - T_C}{T_H} = 1 - \frac{T_C}{T_H} \tag{2.7}$$

where T_C is the temperature on the cold side, and T_H is the temperature on the hot side.

Any real generator will have an efficiency lower than that of the Carnot efficiency, but we see that a greater temperature difference will increase the efficiency. 100% efficiency is only achieved if the cold side temperature reaches $0K$.

In the field of thermoelectrics we operate with a Figure-of-Merit to gain an understanding of the potential of a thermoelectric material. This figure is

given by

$$Z = \frac{\alpha^2 \sigma}{\kappa} = \frac{\alpha^2}{\rho \kappa} \tag{2.8}$$

where α is the Seebeck-coefficient, σ is the electrical conductivity, κ is the thermal conductivity, and ρ is the electrical resistivity.
The factor $\alpha^2\sigma$ is referred to as the power factor and is measured in $\frac{W}{cm \cdot K}$.
The Figure-of-Merit varies with temperature, so it is more convenient with the dimensionless Figure-of-Merit ZT where T is the absolute temperature.

$$ZT = \frac{\alpha^2 \sigma}{\kappa} T \tag{2.9}$$

This ZT shows the performance of the material at a given temperature T. We see that the desired properties are as high Seebeck-coefficient and electrical conductivity as possible, and as low thermal conductivity as possible in order to achieve the highest ZT. The thermal conductivity are split into two contributors, κ_e and κ_l, respectively electrical and lattice thermal conductivity.
Today's thermoelectric bulk materials shows a ZT of around 1 [6], but the goal is to achieve atleast ZT = 3 [10].
The efficiency with ZT included is

$$\eta = \frac{T_H - T_C}{T_H} \frac{\sqrt{1 + ZT_m} - 1}{\sqrt{1 + ZT_m} + \frac{T_C}{T_H}} \tag{2.10}$$

where T_m is the mean temperature between the hot side and the cold side. The conversion efficiencies of these two values of ZT can be seen in figure[2.5].

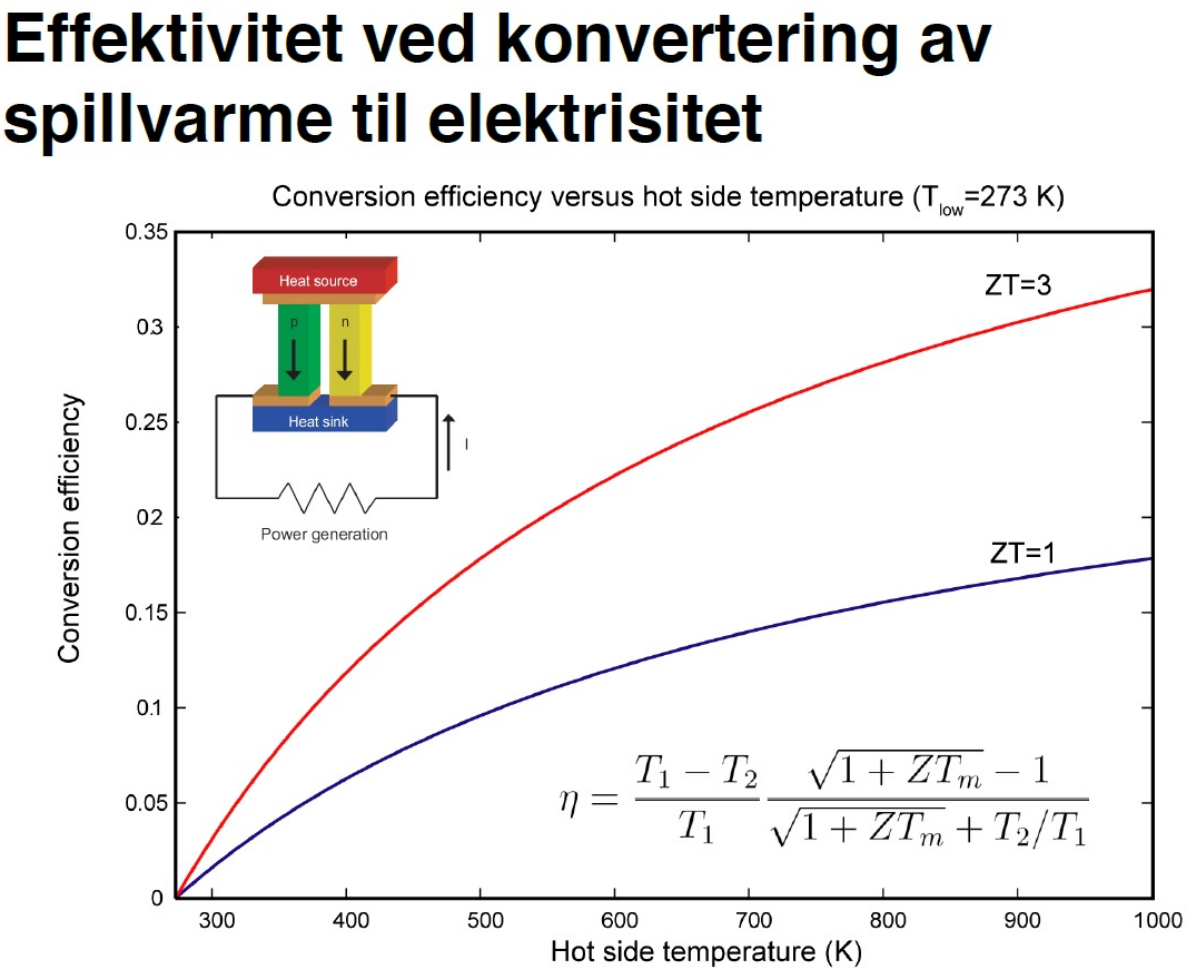

Figure 2.5: Figure title: Conversion efficiency of waste heat to electricity. The difference in efficiency for ZT=1 and ZT=3 at different temperatures. The cold side is held at room temperature. Figure: Øystein Prytz [11]

2.4 Applied Thermoelectric Materials

Because of the low conversion efficiency of thermoelectric materials, they still do not compete on a global energy management level. However, thermoelectricity is used in some products that are commercially available.
Thermoelectric devices are used in a wide range, from systems in need of localized cooling, portable coolers for food and drinks, heat pumps, chargers and light sources where there are no power outlets, and precise temperature measurements to large-scale usage as in spacecraft.

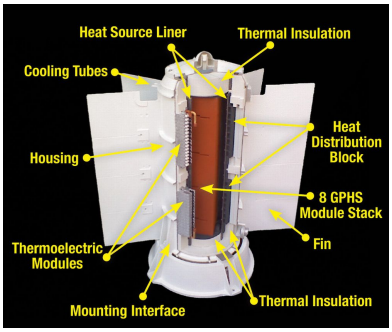

(a) Cassini-Huygens spacecraft uses a radioisotope thermoelectric power generator.

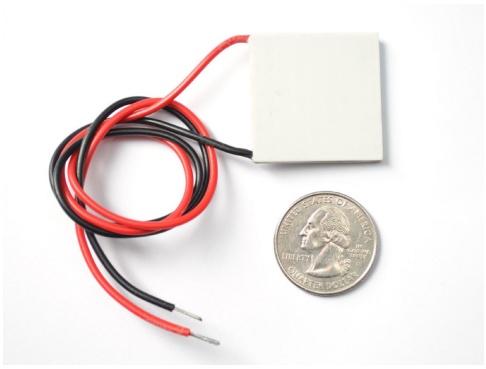

(b) Thermoelectric element for localized cooling.

(c) Portable cooler for food and drinks.

(d) Biolite stove which converts heat from the fire into electricity.

Figure 2.6: A few devices using thermoelectricity

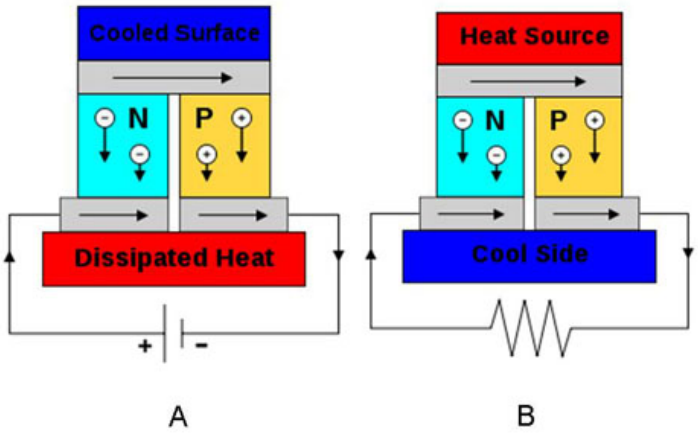

Figure 2.7: A thermoelectric couple. Figure A has an external voltage applied, the electrons will absorb heat at the cooled surface and release the heat at the dissipated heat surface. Figure B has an applied heat source on the top surface while the bottom surface is kept cool. The electrons will turn the received heat into kinetic energy and flow to the bottom where there will be a net build-up of charge, creating a voltage difference.

Thermoelectric modules are built up by many pellets of n-type and p-type semiconductors, sandwiched between ceramic plates. In n-type materials the majority of charge carriers are electrons, while in p-type materials the charge carriers are holes. A pair of one n-type and one p-type pellet is called a thermoelectric couple. A module can be made of one to several hundred couples which are connected electrically in series, and thermally in parallel. They are in contact with each other through typically copper contacts. See figure (2.7). The electrons that have been brought into the conduction band will pass out of the n-type and into the copper, then into the p-type and take the place of a hole.

With an external voltage applied the module is a heat pump, or a cooler depending on the polarity, while with an applied heat source it is a power generator. A DC voltage is needed for the heat pump and the polarity determines the direction of the heat flow, from cold to hot or from hot to cold.

Chapter 3

Introduction to the Half-Heusler system

This chapter deals with the structure of the Half-Heusler alloys. There are many elements that can be combined into a Half-Heusler alloy, mainly metals and semi-metals. In 1903, Fritz Heusler discovered that an alloy with the composition Cu_2MnAl would behave as a ferromagnet even though none of its elements are magnetic by themselves [12] [13]. The family of these alloys are now known as Heusler alloys and have a stoichiometry of 2:1:1. The properties of these alloys can be predicted by counting the valence electrons of the constituent elements [14]. Half-Heusler alloys have a stoichiometry of 1:1:1, they are named Half-Heuslers because they have half the metal atoms of a "full" Heusler. The Half-Heusler version of the first alloy would then be MnCuAl. It is possible to dope a Half-Heusler on all three atom sites, changing the charge carrier concentration, introducing disorder to decrease the lattice thermal conductivity, and tune the band gap [8]. Half-Heusler alloys with a valence electron count of 18 shows semiconducting behaviour, although alloys with a valence electron count of 17 also show narrow band-gaps and promising power factors, such as TiFeSb, which this thesis is about [15] [16].

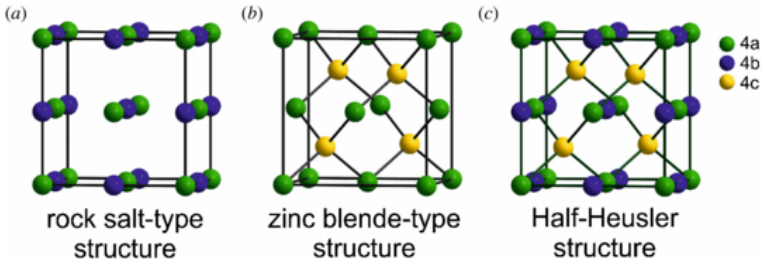

Figure 3.1: Crystal structure of a Half-Heusler. Space group no.216, $F\bar{4}3m, C1_b$. The structure is a blend of a NaCl-sublattice and a ZnS-sublattice

3.1 Crystal Structure

Figure (3.1) shows the crystal structure of a Half-Heusler. The structure has a general formula XYZ and crystallize in a non-centrosymmetric cubic structure (space group no.216, $F\bar{4}3m, C1_b$). The corresponding Wyckoff positions are $4a(0,0,0), 4b(1/2,1/2,1/2)$ and $4c(1/4,1/4,1/4)$. The most electropositive and the most electronegative elements, one of the metals and the semimetal, will form the NaCl-type structure, while the intermediate element will bond to the electropositive element and form the ZnS-type structure. The nomenclature differs in literature on the order of the elements. Some sort the elements alphabetically, others after electronegativity. In this thesis we sort after electronegativity. X is most electropositive, Y is intermediate and Z is most electronegative. MgAgAs is the assigned prototype of all Half-Heusler alloys, but this alloy has a different atomic arrangement than most of the Half-Heuslers. Mg and Ag form the NaCl-structure and Ag and As forms the ZnS-structure. A more suitable prototype would be MgCuSb which crystallizes in the way mentioned earlier in this paragraph. The electropositive Mg and the electronegative Sb forms the NaCl-structure, while Cu bonds with Mg in the ZnS-structure. Then Cu is coordinated by four Mg and four Sb atoms to form an ideal cube [8]. For alloys containing two transition metals the prototype assigned is the LiAlSi-type, which crystallize in the same way as MgCuSb.

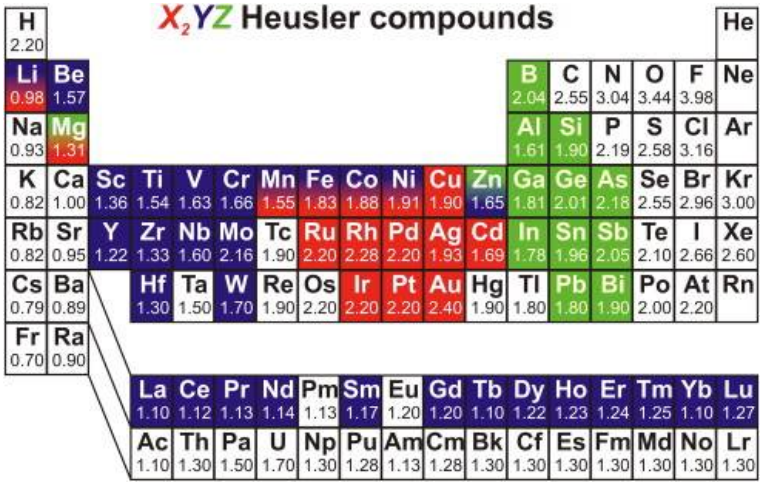

Figure 3.2: Periodic table of the elements colored to see which elements can constitute Heusler and Half-Heusler alloys and their expected positions. X(4a)Y(4c)Z(4b) will be the correct coloring for the wyckoff positions in Half-Heusler alloys. From this we can see that there are several thousands of different combinations for elements in a Half-Heusler alloy.

3.2 Half-Heusler Alloys

As previously said, there are many elements that can form Half-Heusler alloys. Figure (3.2) shows the periodic table with colored elements to show their position in the X_2YZ nomenclature of the Heusler, explained for Half-Heuslers in the caption. Some elements have more than one color, showing that some elements can have different positions depending on the electronegativity of the other elements in the alloy.

There have been made Half-Heusler alloys with up to six elements, where they have substituted half or a quarter of the sites with other Heusler applicable atoms and some dopant. These are the alloys that are the state of the art Half-Heuslers due to their competing ZT with the best of the bulk thermoelectrical materials. See figure (3.3) for comparison.

Half-Heusler alloys are interesting because they can be made using abundant, non-toxic elements, the vast number of different compositions and dopants for tuning the properties, and that they show promise in different fields such as solar cell applications, thermoelectrics, topological insulation,

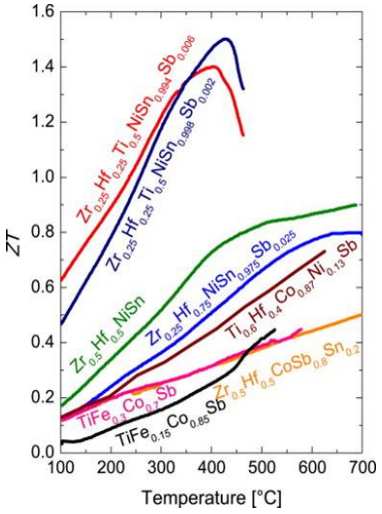

(a) State of the art Half-Heusler compounds. [8]

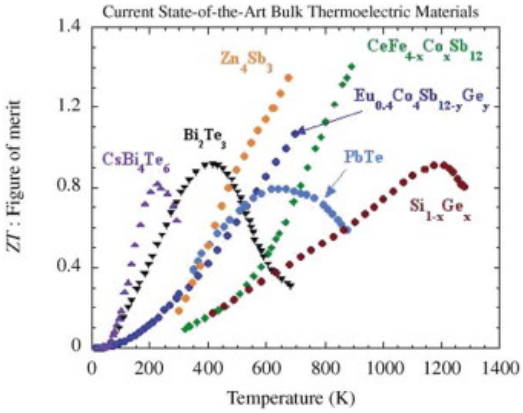

(b) State of the art bulk thermoelectric compounds. [6]

Figure 3.3: Comparison of State of the art Half-Heuslers versus State of the art bulk compounds. Bi_2Te_3 is used for cooling and $Si_{1-x}Ge_x$ is used for power generation. [6]

spintronics and even superconductivity [5]. Figure (3.4) shows a collection of Half-Heusler alloys plotted with their band gaps as a function of average nuclear charge. Also included is the solar energy spectrum to show the great potential for solar cell applications. TiFeSb has been added according to band gap found in [16].

3.3 TiFeSb

In this section we will look at previous work done on the TiFeSb system such as synthesis, sample preparation, structure and properties. There are mostly calculated properties found in literature as the system might have been deemed unimportant due to the fact that it is a Half-Heusler alloy with a valence electron count of only 17, whereas the most studied ones are with a valence electron count of 18. TiFeSb is expected to be p-type due to this electron deficiency and from the work of [7]. It has a lattice parameter of $a = 5.957$Å and a density of $\rho = 7.09\frac{g}{cm^3}$.

Figure 2 from F Casper et al 2012 Semicond. Sci. Technol. 27 063001

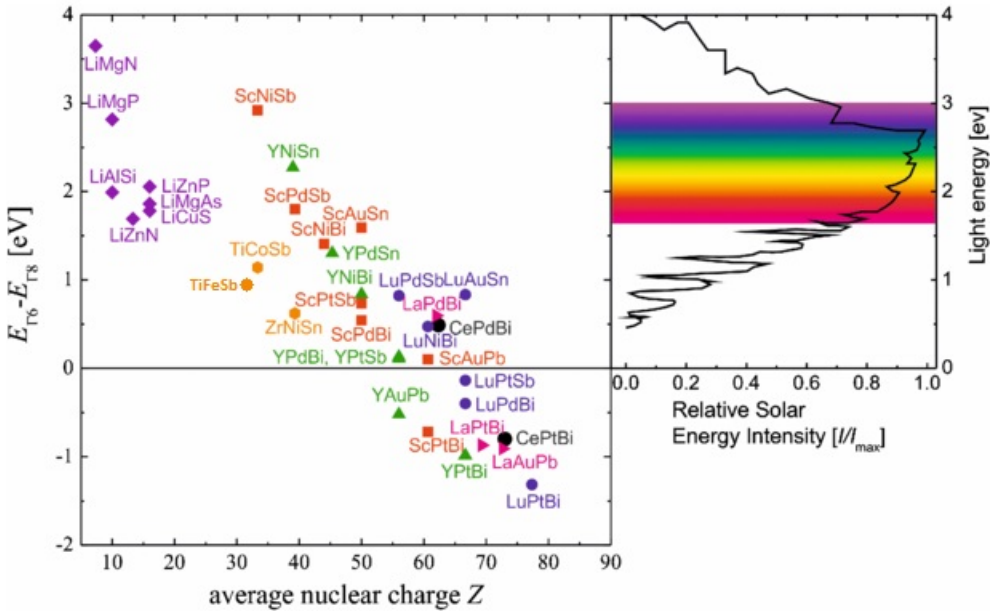

Figure 3.4: Band gaps as a function of their average nuclear charge (Z) for various Half-Heusler and Nowotny-Juza phases calculated using the optimized lattice parameter. The solar energy spectrum is shown to emphazise the great potential for solar cell applications [5].

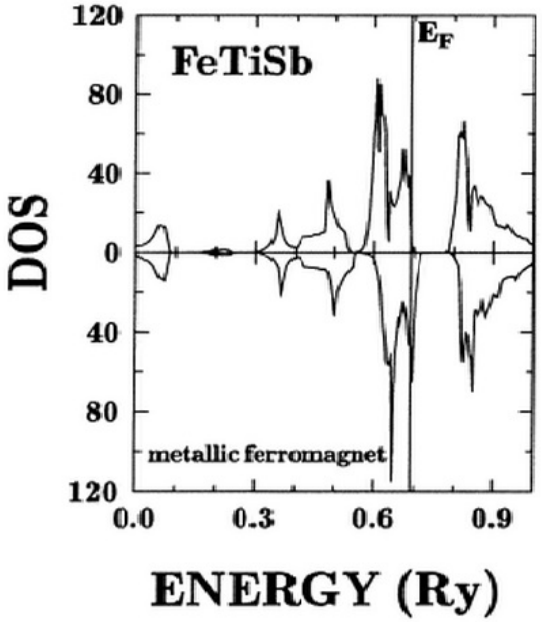

Figure 3.5: Density Of States (DOS) for TiFeSb. We see the Fermi level enters the valence band, predicting it will be a p-type. 0.07Ry = 0.95eV

TiFeSb is described as a metallic ferromagnet, with the Fermi level entering the valence band, predicting that it will show p-type metallic properties. It is also reported to be a paramagnet in that it is attracted by an external magnetic field. The band gap is reported to be $0.9 - 1.0$eV (figure 3.5) [15] [16]. The energy gap arises essentially from the hybridisation of d states coming from different transition-metal atoms and the p states on Sb. The DOS above the gap is dominated by d states on Ti, overlapping with d states on Fe. Electronic states lying just below this gap are dominated by d states on Fe, being hybridized by d states on Ti, and p states on Sb. The lowest-lying electronic states apart from the valence band correspond mostly to s states on Sb [17]. The authors of ref. [18] report from a refinement of the diffraction data that TiFeSb shows a more complex crystallographic structure, a super-cell or disordered structure, than a regular Half-Heusler. When assuming a disorder on X sites within the X_2YZ-type structure of a Heusler alloy, the KKR-CPA computations show a non-magnetic ground

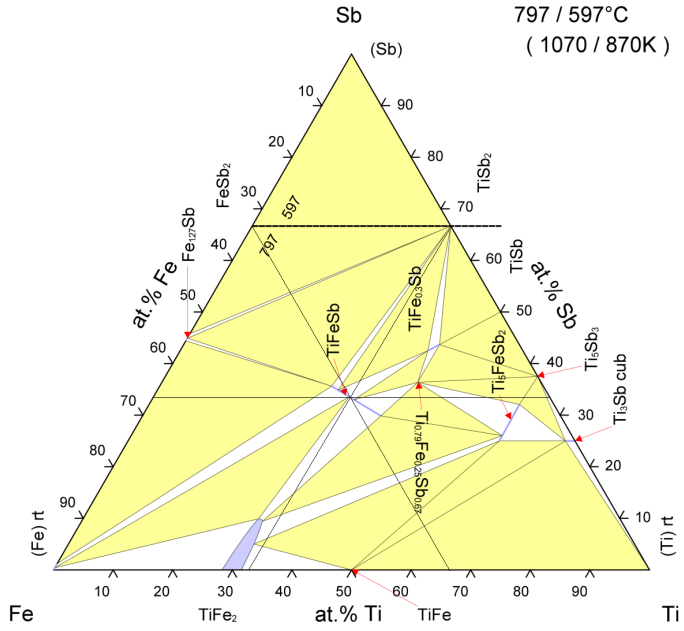

© ASM International 2009. Diagram No. 203024

Figure 3.6: The phase diagram of TiFeSb. Thin black lines drawn in for the 1:1:1 stoichiometry.

state of $(Fe_{0.5}E_{0,5})_2TiSb$, where E denotes a vacancy, which agrees with their experiments.

The phase diagram of TiFeSb is shown in figure (3.6). Blue areas are single phase, yellow areas are two-phase and white areas are three-phase fields. The line at the TiFeSb composition is a monovariant curve.

The most common method to synthesize bulk Half-Heusler compounds is to use an electric arc-melter. Stoichiometric amounts of the high-purity elements are added to a water-cooled copper crucible and melted. The melting process takes a few seconds, but the ingots needs to be turned over and remelted several times to ensure a homogeneous element distribution throughout the sample. One can also take out the cooled ingot and hand-crush it in a piston, then remelting it to ensure a homogeneous sample.

Special care has to be taken to avoid oxygen contamination. Therefore the melting is done inside a glass bowl with vacuum, where Argon is pumped in for an inert atmosphere. One can also use an oxygen getter, such as Ti or Ta, to further improve the sample quality. A few more rounds of flushing with argon then pumping for vacuum can also be efficient.

The phase purity as well as the crystal structure can be improved by annealing the ingot or the crushed sample in a sealed silica tube. In general high temperatures for the annealing process is preferred due to increased diffusion velocity and that impurities vanish more easily. Rapid quenching in ice water is then performed and may further the chances of the desired structure. The samples can then be crushed in a mortar or ball-milled depending on the wanted grain sizes, and sintered into a solid piece. For desired dimensions of samples for different measurements, the samples can be ground and polished by sand-paper and polishing disks.

Not much can be found on the thermoelectric properties of a pure TiFeSb alloy. The authors of [19] state that TiFeSb is interesting because of the low thermal conductivity, and that it can be further reduced by Mn-doping. This may be good for the research community to finally get a full view of the properties of an undoped TiFeSb alloy with this thesis.

Chapter 4

Experimental methods

This chapter will give an overview of the synthesis process, with melting of the compounds, further treatment for structural refinement, and the preparation of the samples for measurements. We will also see the methods of characterizing the structure and the thermoelectric properties.

We used the same methods for all samples, but varied the time and temperature aspect in different parts of the process. Annealing and sintering are used to minimize impurities and occurrence of unwanted phases. The structural characterization techniques used are X-ray diffraction (XRD) and a Scanning Electron Microscope (SEM) to determine the composition of the samples and to see if we have some phases that are richer in one or more elements than other sites, which can influence the properties. Lastly, the most important and the main job of the thesis, is to measure the thermoelectric properties. Thermal and electrical conductivities and the Seebeck-coefficients, the set-up of these measurements and the variables. We used a custom set-up for both Seebeck measurements and the first Van der Pauw measurement, then a automatic procedure for Van der Pauw measurements of both samples at the MiNa-Lab together with Hall measurements for both samples. Thermal conductivity was measured by the Laser Flash method at MiNa-Lab.

4.1 Synthesis

There are different methods used for the synthesis of Half-Heusler alloys, mostly used is electric arc-melting followed by spark plasma sintering [8], some have used a melt-spinning process [20], or even levitation melting [21]. The melt-spinning produces ribbons with nano-dimensions, but there can be a difference in structure on the side that was touching the copper-barrel and the side of the ribbon that was not. Levitation melting leaves out the part where you need to turn your sample over for an even melt, and also protects the alloy in case it would react with the crucible the compounds are held in during the melting process. The constant flow of molten metal as it levitates will also mix the compounds better, resulting in improved homogeneity [22].

High-purity compounds are needed, preferably not powders, as they might sublimate and result in a non-stoichiometric sample. We where mostly worried about Sb disappearing from the mix, so we used chipped pieces of Sb, and tried to cover the pieces with the Fe and Ti. Ti was cut from wires and Fe was in filings. The melting point of Sb is almost 1000K below Ti and Fe, and the boiling point of Sb is only 90K above the melting temperature of Ti (Sb: melt=904K, boil=2023K, Ti: melt=1933K). However, there was no trace of a significant amount of Sb being sublimated to the glass bowl of the arc-melter.

4.1.1 Method of Synthesis

The melting of the ingots took place at IFE (Institutt for Energiteknikk) at Kjeller outside Oslo.

Figure (4.1) shows the set-up for the melting of the ingots. Raw materials are placed in one of the crucibles and a titanium ball is placed in an adjacent crucible. Figure (4.1) (b) shows a bigger crucible on the front side, but without the possibility of combining with a titanium ball. This crucible also has a higher position when turned upright so care has to be taken so the cathode rod does not relax into the ingot if it is released. We only used the crucible shown in the figure. The crucible is made of copper and is water-cooled. The

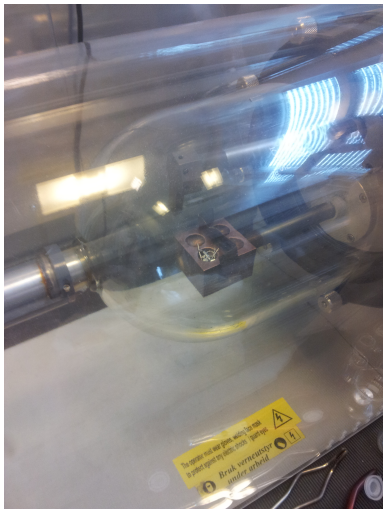

(a) The electric arc-melter with raw materials in the bottom left crucible. The glass bowl is pumped for vacuum and an argon atmosphere is introduced.

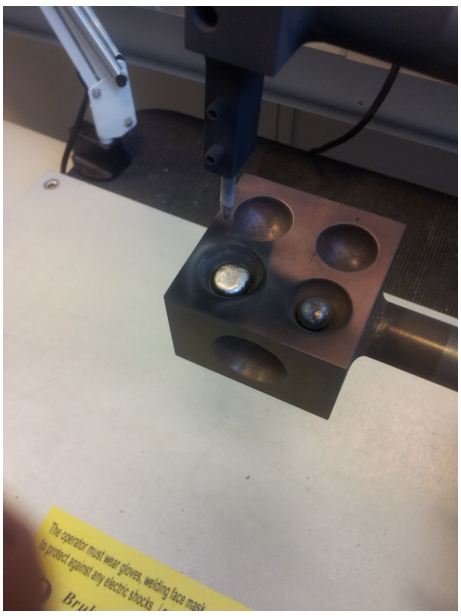

(b) The melted ingot to the left and a Titanium ball to the right to pick up stray oxygen.

Figure 4.1: The electric arc-melter.

cathode produces a high-voltage current aimed directly at the materials.

The procedure of use for the melter is to load in your materials, then fix the bowl to the rest of the machine with nuts, not too tight or else there might be strain on the bowl. The bowl reaches a bit further in than the ring with the screws and nuts, and the occurrence of vacuum shows that it is tight. Cooling water is turned on and checked for flow. Vacuum is pumped first, then Argon in pumped in. The bowl is flushed with Argon and subsequent vacuum pumping 3-4 times to ensure that all oxygen is out of the system. The voltage source is switched on and is only on for the duration of the melting. Safety equipment includes gloves to protect from heat and shocks, and a shaded visor to protect eyes from the bright spark of the cathode.

The melting itself only takes 5-10 seconds for each side of the ingot. First the materials are melted until everything collects into a ball. Then the cathode rod is used to push the ingot to the edge of the crucible so a part of it is over the edge. A quick push on the part sticking out will turn the ingot for melting on the other side. After successful melting on both sides, the sample is taken out and crushed for remelting. In the time it takes to unscrew the bowl, the ingot will be cold to touch. We crushed the ingot 2 times for a total of 3 full melting processes. The crushing helps for new contact surfaces for diffusion and makes the ingot more homogeneous.

4.1.2 Raw Materials and Composition

Raw materials used for this work is as follows:

Titanium

Koch-Light Laboratories LTD, 99.9%
$47.867\frac{g}{mol}$, $\rho = 4.54\frac{g}{cm^3}$
Wire

Iron

Sigma-Aldrich, 99.99%
$55.845\frac{g}{mol}$, $\rho = 7.874\frac{g}{cm^3}$
Filings from a rod

Antimony

Alfa-Aesar #000030, 99.99%
$121.760\frac{g}{mol}$, $\rho = 6.691\frac{g}{cm^3}$
Chipped ingot

The first pair of samples where made with an aim of getting ingots of around 3g. This was decided so that all sample material could fit in the crucible and be melted at the same time. However, we where worried that a sample of 3g would give too little powder for sintering, so we combined the two samples into one before annealing and sintering.
The second pair of samples where made to get samples of 5g. Due to the amount of material exceeding the holding capability of the crucible, these samples where melted half a sample at the time, which my supervisor at IFE had found to be equally successful with other alloys of different material systems. Both the first two and second two pairs of samples had some discolouring, while we didn't remove it from the first two, we removed it from the second two by grinding with an electric drill with a grinding tip.

Table 4.1: Calculations of sample compositions

Sample no.	Element	Mol	New mol	Calc. weight [g]	Weighed [g]	Sample weight [g]
1	Ti	0.0133	0.0139	0.667	0.667	
1	Fe	0.0133	0.0139	0.778	0.779	
1	Sb	0.0133	0.0139	1.692	1.691	3.1371
2	Ti	0.0133	0.0143	0.686	0.686	
2	Fe	0.0133	0.0143	0.798	0.798	
2	Sb	0.0133	0.0143	1.741	1.769	3.2537
3	Ti	0.02218	0.02218	1.061484	1.0614	
3	Fe	0.02218	0.02218	1.238402	1.2384	
3	Sb	0.02218	0.02218	2.700114	2.7001	4.9999
4	Ti	0.02218	0.02218	1.061484	1.0615	
4	Fe	0.02218	0.02218	1.238402	1.2385	
4	Sb	0.02218	0.02218	2.700114	2.7002	5.0002

The weighing process of the first two samples was done by calculating the mol-weight according to a 3g-sample, weighing in Titanium until close to the calculated weight, then calculating a new mol-value based on the weighted Titanium. The latter two 5g samples where weighted accurately based on the calculated mol-weight.

The scale used to weigh the materials where accurate to within the 4th decimal, but fluctuated a little. It was for some reason more stable for samples 3 and 4, the reason could be that the raw materials where in finer pieces than the first two samples.

To use sample 3 as an example, the calculation where as follows:

Mol for a 5g sample

$$Mol = \frac{weight[g]}{Z_{Ti}+Z_{Fe}+Z_{Sb}[\frac{g}{mol}]} = \frac{5g}{47.867+55.845+121.760\frac{g}{mol}} = \frac{5g}{225.472\frac{g}{mol}} = 0.02218mol$$

Titanium

$$47.867\frac{g}{mol} \cdot 0.02218mol = 1.061484g$$

Iron

$$55.845\frac{g}{mol} \cdot 0.02218mol = 1.238402g \qquad = 5.000000g$$

Antimony

$$121.760\frac{g}{mol} \cdot 0.02218mol = 2.700114g$$

4.1.3 Annealing and Grain-size control

The annealing was done in evacuated and sealed pyrex glass-tubes, in a standing barrel furnace. Pyrex glass was used so that the sample wouldn't adhere to the walls of the tube, and the glass doesn't expand when heated or contract when cooled. After annealing the tubes are carefully lowered into a bucket of water for rapid cooling. A rapid cooling helps to maintain the small grain size that is desired. Slower cooling will give a chance for larger crystallites to grow, which can result in non-uniform phases.
The annealing will break the bonds of unwanted phases, help diffusion and will allow more of the sample to form the Half-Heusler phase. To further help the diffusion the samples where crushed in a stamp first, then in a mortar, making small grains, thereby making many contact areas and shortening the diffusion length. The latter two samples where crushed more thoroughly in the mortar than the first.

The combined samples 1 and 2 where annealed at $700°C$ for two weeks,

while samples 3 and 4 where annealed at $900°C$ for 13 days.

After the annealing process and following quenching, the tubes are smashed open and the contents where emptied in a mortar to examine the powder for large grains. The powder is then cold pressed into a pellet at 5 tonnes pressure before sintering.

The tube containing sample 4 had cracked at the top of the powder, making a small amount of water seep in and contaminating the powder. If this happened during annealing or during quenching, we are not sure, but the powder was discarded and not prepared as a sample.
The tube with sample 4 was lowered into the barrel furnace before sample 3, and it touched the bottom before it was released so only the top of the tube hit the wall of the furnace, making it unlikely that it cracked at this point. The furnace is relatively narrow, so the two tubes of samples is resting in a way that the top tube is balancing on top of the other and leaning against the wall. As sample 3 was lowered into the furnace they might have collided with enough force to crack the glass, but still this is done very carefully and there has to be considerable force to crack these tubes. The option left is that it cracked as it was lowered into the bucket of water for quenching. The tube with sample 3 was lowered in first and released a few centimeters above the bottom of the bucket, and it was fine. The tube with sample 4 was then lowered into the water, and released at the same height. The tube hit the bucket bottom first, so if there would be any cracks, it should have been there. The crack was not evident before the samples had cooled and was picked out of the water. A little more on this is in the synthesis part of the result chapter.

4.1.4 Sintering

For the sintering, the pressed pellet is put inside a cylinder with a piece of felt on both sides. It is also packed with graphite powder around the pellet. Vacuum is pumped to below 0.1mbar, and the heating is switched on. The

combined sample was sintered at $700°C$, while sample 3 where sintered at $900°C$. See figure (4.2) for the sintering steps.

Figure (4.3) shows the sintering instrument. The pressure used is $100\frac{kg}{cm^2}$ and the cylinder has an area of $16cm^2$, and a diameter of $2.54cm \Rightarrow r = 1.27cm$. This gives a pressure of:

$$\frac{1600kg}{\pi 1.27^2 cm^2} = 315.76\frac{kg}{cm^2} \Rightarrow 30.965Pa \tag{4.1}$$

The pressure is slowly reduced one hour after cooling starts.
Sintering is used to get a compact sample which can be manipulated without crumbling to pieces.
After the sintering is done, the preparation of the samples for measurements begin.

4.1.5 Sample preparation, Geometry and Physical Measures

The samples are prepared for measurements by grinding them with different sandpapers into the shape and size required for the different instruments. The samples are glued onto metal cylinders and are ground starting with a coarse sandpaper, then moving on to finer and finer papers. We started out with a x500 paper, then continued with a x1200 paper before finishing with a polishing paper of x4000. The polishing is most important for the microscopy examination, but the other measurements also requires a polished and plane surface for accurate measurements. Figure (4.4) gives a schematic of the sample geometries.

Laser Flash for thermal conductivity and the Seebeck measurements require a little thicker samples than the sample size for the electrical measurements. The reason is that for Laser Flash we measure diffusivity which require some material for the laser to diffuse through. For the Seebeck measurements it is required that we are able to keep the top and the bottom of the sample at a temperature difference for the Seebeck effect to work. Van

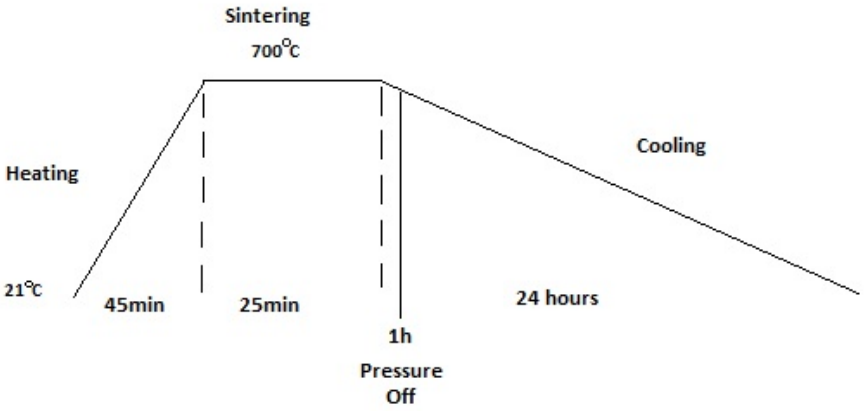

(a) Schematic of the sintering process of the combined sample

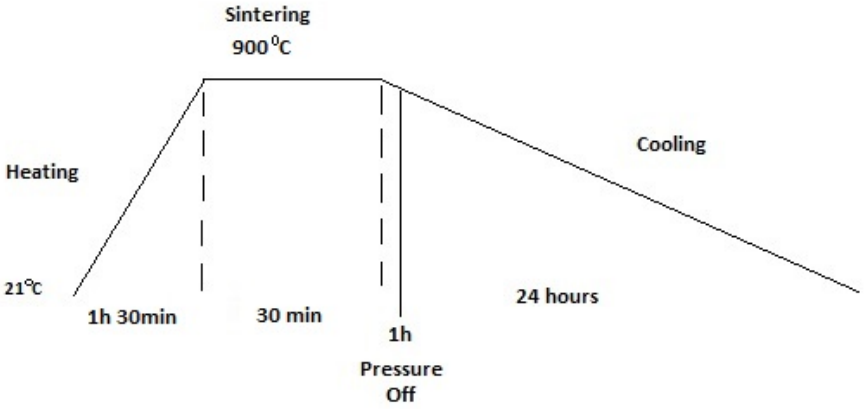

(b) Schematic of the sintering process for sample 3

Figure 4.2: Schematics of the sintering profiles.

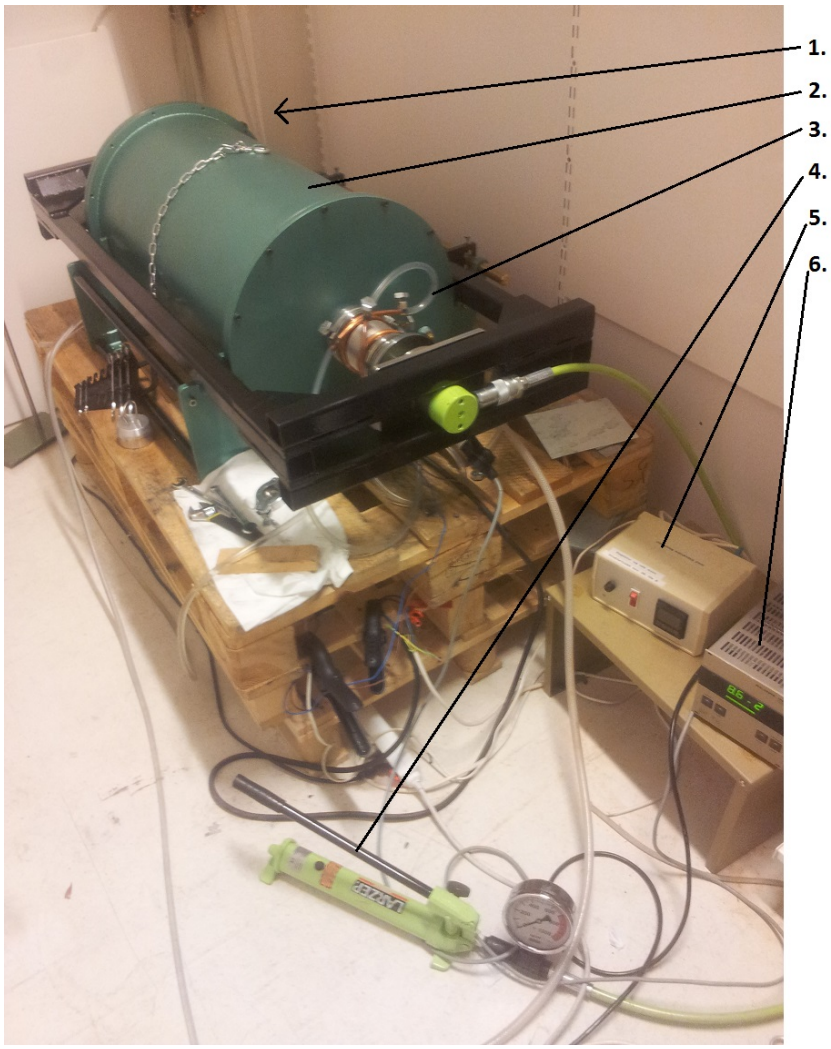

Figure 4.3: The sintering instrument. 1: Vacuum pump (behind the instrument), 2: Sintering barrel, 3: Water cooling, 4: Pressure, 5:Temperature controller, 6: Vacuum monitor.

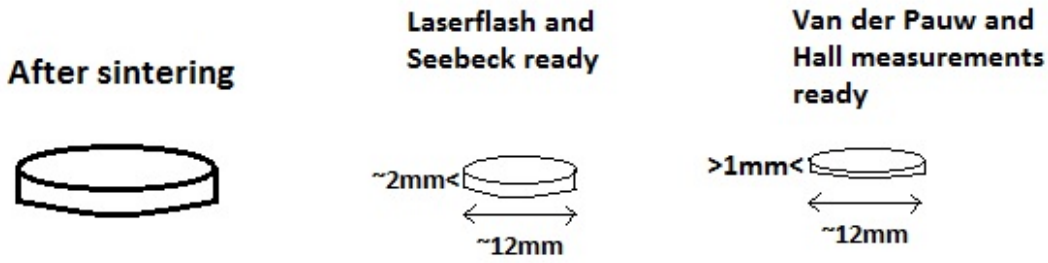

Figure 4.4: Schematic of the sample size and geometry required for the different measurements

der Pauw and Hall measurements assume that the sample is very thin, or atleast much thinner than the other dimensions of the sample. The assumption is that the electrical field is a flat line from one end to the other, while a thicker sample will have field lines that curve deeper into the sample and will affect the measurement.

4.2 Structural Characterization

To get information on the present phases and if we managed to make a Half-Heusler alloy, the samples are examined by X-Ray Diffraction (XRD) and viewed in a Scanning Electron Microscope (SEM).
XRD gives a fingerprint of the samples which can then be compared to a database to identify the compound. It is also possible to calculate an XRD pattern using different programs in case the structure cannot be found in databases.
SEM was used to look at the microstructure of the samples. From this we can see if there are certain phases that are richer in some elements than others, and how they are dispersed through the sample.

The microscope uses backscattered electrons and secondary electrons. The secondary electrons comes from the surface, while the backscattered electrons goes deeper into the sample. The quantity of backscattered electrons are proportional to the atomic number, therefore heavier elements will be seen as lighter areas in the sample. An SEM can also be used to find the composition of areas in the samples. This is done by detecting X-rays that are sent out because electrons in the sample will be excited from collisions by incoming electrons, and electrons from outer shells will relax to lower shells and take their place and send out characteristic X-rays. This method is called Energy-Dispersive Spectroscopy (EDS).

4.2.1 XRD

In an XRD analysis a small piece of the sample is ground into a powder and spread evenly on a glass plate. This is to ensure that the X-rays hit grains at many different angles and reflect off different planes. We will see peaks in the X-ray pattern with different positions and intensities. The intensity comes from how often an X-ray is reflected from a certain plane, while the positions of the peaks are determined from the unit cell.
Figure 4.5 shows a calculated XRD profile from Pearson's crystal database for TiFeSb. We need to calibrate the peaks to fit our experimental XRD pattern in case there are some systematic errors in the pattern. This is done by adding silicon powder to the sample powder before sending the sample to X-ray analysis. Silicon is used because of its distinguishable peak positions and intensities.

4.2.2 SEM

The Scanning Electron Microscope produces images by scanning a focused electron beam across the surface of the sample. The electrons interact with the atoms in the sample and produces different signals that can be detected and used to form an image. The signals produced are Secondary electrons, Backscattered electrons, characteristic X-rays, and cathodoluminescence. The signals comes from interactions between the electrons and the

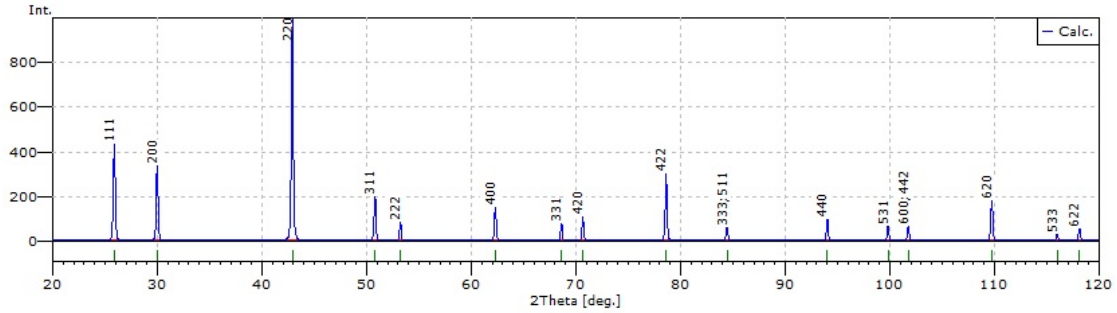

Figure 4.5: TiFeSb XRD profile from Pearson's crystal database. The peaks are labeled with the planes they originate from.

atoms near the surface of the sample. The secondary electrons can produce high-resolution images showing details of nanometer size. The narrow electron beam also gives the SEM a good field-of-depth giving a 3D-view of the surface of the sample.

Backscattered electrons are electrons from the beam that are reflected elastically from the sample. The intensity of the backscattered electrons are related to the atomic number of the atoms present in the sample, so lighter atoms appear darker in the image and heavier atoms appear lighter. Characteristic X-rays are emitted when the electron beam removes an inner shell electron from the sample, causing an electron with higher energy to take its place by releasing energy. These X-rays are then used to identify the composition of the sample.

Figure 4.6 (a) shows the microscope used in this thesis, and Figure 4.6 (b) shows where in the sample the different signals are produced.

All samples must also be of an appropriate size to fit in the specimen chamber and are generally mounted rigidly on a specimen holder called a specimen stub. The samples must be electrically conductive and are grounded to the specimen stub with conducting carbon tape. This is to prevent a build-up of charge at the surface which may distort the images, making areas lighter and lighter, and repelling other incoming electrons. One can also apply a thin coating of a conducting material, typically used is car-

(a) Hitachi TM3000 tabletop microscope.

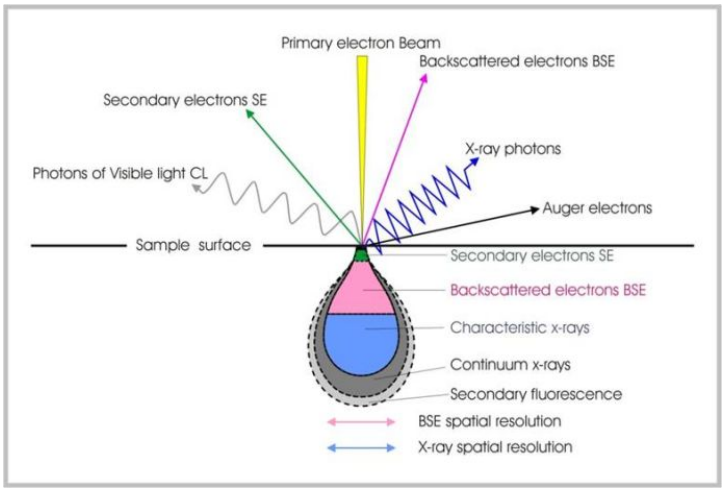

(b) Different signals produced and where they originate. Photo: http://www.gla.ac.uk/media/media_249720_en.jpg

Figure 4.6: (a) Tabletop SEM. (b) Signals detected and used.

bon coating. Metallic samples requires little preparation other than cleaning and polishing.

4.3 Electrical Characterization

In this section we will go through the measurement set-ups for the different measurements. To calculate the ZT of our thermoelectric material we need to know the thermal conductivity, electrical resistivity and the Seebeck-coefficient. Thermal conductivity is measured by the laser flash method, electrical resistivity is measured by the Van der Pauw method, and for the Seebeck-coefficient we used a custom set-up which measured the voltage produced when the sample was subjected to a temperature difference.

We also did Hall measurements to get the charge carrier concentration and mobility. The Hall measurement uses the same set-up as the Van der Pauw measurement, only with an applied magnetic field and it measures diagonally across the sample.

4.3.1 Thermal Conductivity: Laser Flash Measurements

The thermal conductivity is determined by:

$$\kappa(T) = \alpha(T)\rho(T)C_p(T) \tag{4.2}$$

Where α is the thermal diffusivity and C_p is the specific heat. These two are measured. ρ is the density of the sample which is entered in the program as a parameter.

The sample is prepared as a disk and mounted inside the instrument in a holder. Before the measurement we coated the sample with carbon to help the detector to detect the infrared signal on the backside of the sample. The instrument is cooled with liquid nitrogen at a flow of 100 ml/min.

The laser pulses a beam onto the surface of the sample, and the energy is transferred through the sample and emitted on the backside. The detector will then detect this heat as infrared radiation. Figure 4.7 shows a schematic of the Laser flash measurement. The measurement was done every 50°C from

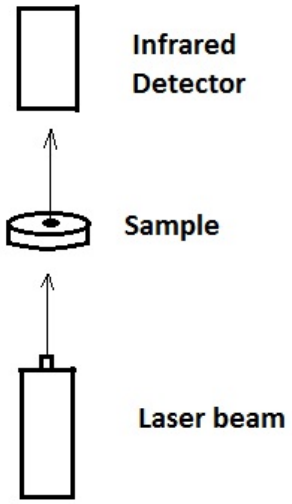

Figure 4.7: Schematic of the Laser flash measurement

50°C to 500°C. At the same time we mounted a pyroceram sample in another sample holder next to our sample. This pyroceram sample, with a known specific heat, is used to determine the specific heat of our sample. The Cape Lehmann + pulse correction model is used to account for heat loss and finite pulse-effect.

Figure 4.8 shows the instrument used at MiNA-lab for the laser flash measurements [23].

The thermal conductivity is split into two contributing factors, κ_l which is the lattice thermal conductivity, and κ_e which is the electrical thermal conductivity. κ_l is from phonons which is lattice vibrations and κ_e is from electrons which carry heat, and can be calculated by Wiedemann-Franz law

$$\frac{\kappa_e}{\sigma} = LT \tag{4.3}$$

Where σ is the electrical conductivity, T is the absolute temperature and L is the Lorentz number given by $L = \frac{\pi^3}{3}\left(\frac{k_B}{e}\right)^2 = 2.44 \cdot 10^{-8}\mathrm{W\Omega K^{-2}}$.
It is assumed that the phonons are the main contributors to the thermal

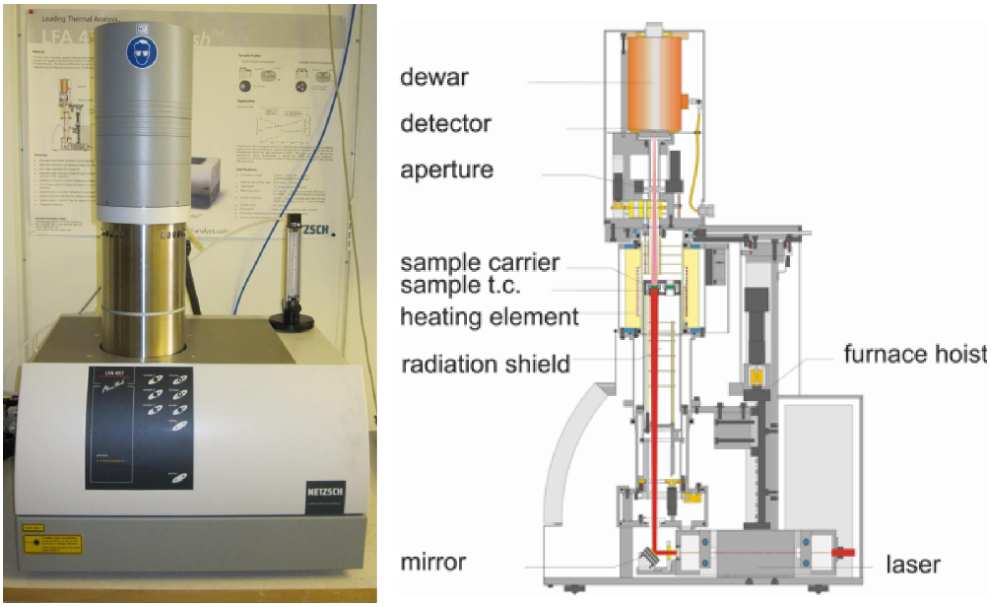

Figure 4.8: NETZSCH LFA 457 Microflash equipment. The thermal conductivity is found by measuring the heat propagation through the sample after heating one side with the laser.

conductivity, but from the Wiedemann-Franz law we see that the thermal conductivity is proportional to electrical conductivity, since free electrons carry both electrical and heat energy. Still the phonons are more important, and as an example we can mention that silver has a high electrical conductivity, but has a lower thermal conductivity compared to diamond, which is an insulator. This is because diamond has a very ordered structure, making it a very good conductor of phonons.

4.3.2 Van der Pauw Resistivity and Hall Measurements

The Van der Pauw method is used to find the resistivity of the material, while Hall measurements are used to find the charge carrier density, the mobility of the majority charge carrier, and whether the material is p-type or n-type. The measurement is a 4-point technique and has these conditions:

- The sample must have a flat shape of uniform thickness.
- The sample must not have any isolated holes.

- The sample must be homogeneous and isotropic.
- All four contact points must be at the edges of the sample.
- The area of contact of any contact should be at least an order of magnitude smaller than the area of the entire sample.

See Figure 4.4 for sample geometry. The sample needs to be much thinner than its width and length, and to reduce errors the sample is preferred to be symmetrical. In addition to the contacts being placed as far out on the edges as possible and that they are as small as possible, they should be made from the same batch of wire to reduce thermoelectric effects, and of course be of the same material.
Figure 4.9 shows a schematic of the set-up and the sample holder for the Van der Pauw and Hall measurements. Beginning at the top left contact, the contacts are numbered 1-4 in a counter-clockwise direction. We run a current through contacts 1 and 2, I_{12}, and a voltage is measured between contacts 3 and 4, V_{34}. From these points we get the resistivity R_{12-34}. This is done for all contact points. The current direction is reversed and another measurement cycle is performed. The instruments used are $KELTHLEY$ 7001 switch controller, $KELTHLEY$ 2182A voltmeter and $KELTHLEY$ 6221 DC and AC current source.
The reciprocity theorem shows that $R_{AB,CD} = R_{CD,AB}$, therefore it is possible to obtain a more precise value of the resistivities R_{12-34} and R_{23-41} by making measurements of their reciprocal values R_{34-12} and R_{41-23} and averaging the results.

We can denote the entire measurement cycle as follows

Denotation of resistances

$$\begin{aligned} I_{12} &- V_{34} \rightarrow R_{12-34} \\ I_{23} &- V_{41} \rightarrow R_{23-41} \\ I_{34} &- V_{12} \rightarrow R_{34-12} \\ I_{41} &- V_{23} \rightarrow R_{41-23} \end{aligned}$$

Reversing the current

$$
\begin{aligned}
I_{14} &- V_{32} \rightarrow R_{14-32} \\
I_{21} &- V_{43} \rightarrow R_{21-43} \\
I_{32} &- V_{14} \rightarrow R_{32-14} \\
I_{43} &- V_{21} \rightarrow R_{43-21}
\end{aligned}
$$

The sheet resistivity we are after can be determined by the two characteristic resistances R_A and R_B, where R_A are all vertically measured resistivities and R_B are all horizontally measured resistivities. Then we take the mean value of these resistivities to use them in the Van der Pauw equation 4.6.

$$R_A = \frac{R_{12-34} + R_{34-12} + R_{21-43} + R_{43-21}}{4} \tag{4.4}$$

$$R_B = \frac{R_{23-41} + R_{41-23} + R_{32-14} + R_{14-32}}{4} \tag{4.5}$$

The sample holder allows for resistivity and Hall measurements for a temperature range. It is also connected to a vacuum pump and a temperature controller. The measurements are done at a temperature range of 50°C to 450°C with a heating rate of $10\frac{K}{min}$ between each measurement.
The contact wires are fastened to the edge of the sample with silver epoxy. The epoxy is one part bright silver epoxy and one part grey silver hardener. Both parts are mixed in equal amounts. We heated the system up to 100°C for the epoxy to cure, then lowered the temperature to 50°C before starting the measurements. After mounting the sample, the lid is fastened with screws in the corners of the casing, and the system can be placed in a magnetic field as shown in Figure 4.9 (c). For opposite B-field direction the magnet is turned up-side down and the system is placed back in.
The epoxy is named 2400 Circuit works conductive epoxy, and according to the technical information sheet, it has a resistivity below $1.0{\cdot}10^{-5}$ Ohm·m.

The Van der Pauw equation is

$$exp\left(-\pi\frac{R_A}{R_{Sheet}}\right) + exp\left(-\pi\frac{R_B}{R_{Sheet}}\right) = 1 \tag{4.6}$$

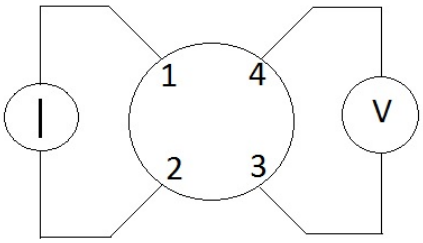

(a)

(b)

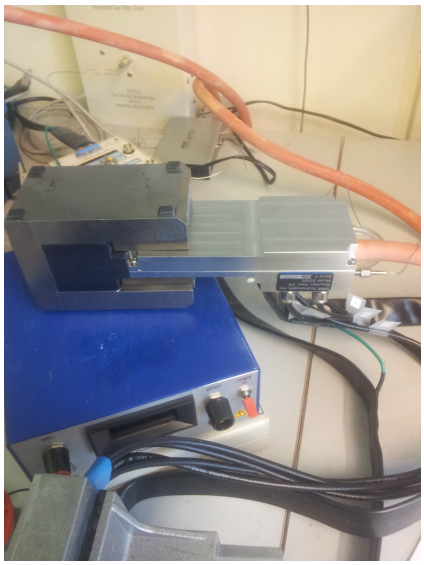

(c)

Figure 4.9: Van der Pauw method: Figure (a) shows a schematic of the set-up for a Van der Pauw measurement. Current is run through two contacts and a voltage is measured between the two other contacts. This is done for the full circle. Figure (b) shows the sample holder. The sample is placed on the white square, and the thin wires barely visible in the corners are placed on the edge around the sample and secured in place by silver epoxy. Figure (c) shows the sample holder placed in the magnetic field of 0.5T.

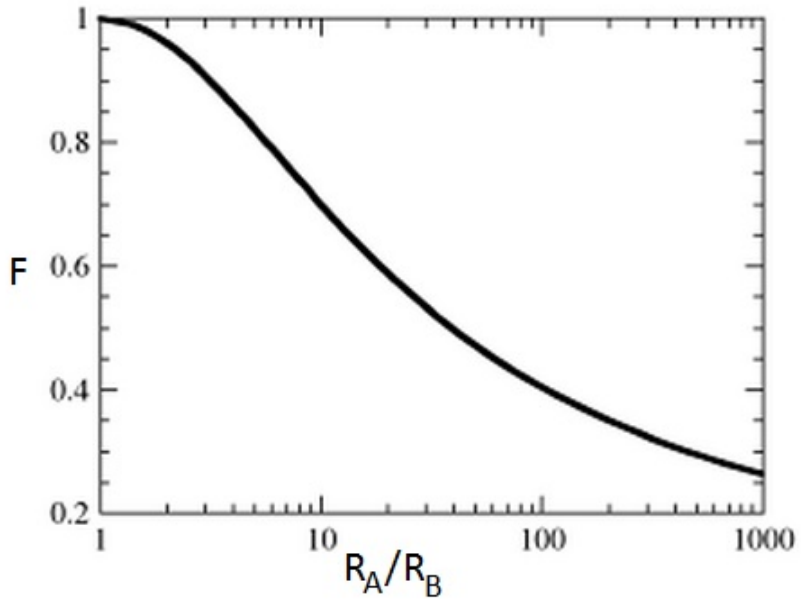

Figure 4.10: The universal F-function used to calculate the sheet resistance in the Van der Pauw method. $F = 1$ if $R_A = R_B$ [24]

where R_{Sheet} is the sheet resistivity given by $R_{sheet} = \frac{\rho}{t}$ where ρ is the resistivity[Ωm] and t is the sample thickness in meters.

The solution to the Van der Pauw equation can be written as

$$R_{Sheet} = \frac{\pi}{ln2}\frac{R_A + R_B}{2}F\left(\frac{R_A}{R_B}\right) \tag{4.7}$$

Here, the F-function is a universal function of the ratio between R_A and R_B, beginning at 1 for $R_A = R_B$, and lowering for increased ratios, see Figure 4.10. At the special case of $R_A = R_B$ the solution reduces to

$$R_{sheet} = \frac{R\pi}{ln2} \tag{4.8}$$

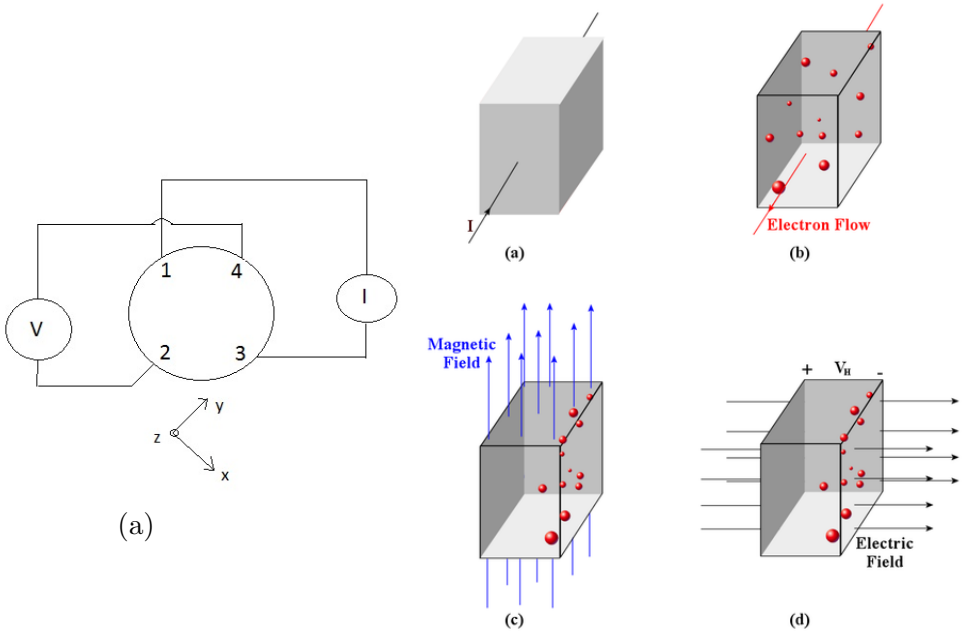

Figure 4.11: Figure (a) shows a schematic of the set-up for Hall-measurements. Current runs in x-direction, creating an induced electrical field created in y-direction, with the magnetic field in z-direction. Figure (b) shows: (a) Current going in x-direction. (b) Electrons flowing because of the current. (c) Electrons gathering to one side because of the Lorentz force from the magnetic field. (d) The induced electrical field in y-direction and the Hall voltage that arises. [25]

For the Hall-measurements we use the same set-up as the Van der Pauw measurements. The difference is an applied magnetic field, and that the current input goes across the sample, for example I_{13} – V_{42}. From these measurements we get the charge carrier concentration, charge carrier type and the mobility of the majority charge carrier. See Figure 4.11 for set-up and what happens in the sample.

In a magnetic field, the charge carriers will experience a Lorentz force

$$\vec{F} = q\vec{v} \times \vec{B} \tag{4.9}$$

Since the current runs in the x-direction, the induced electrical field will be in the y-direction, using the right-hand rule. The electrical field is given by

$$E_y = v_x B \tag{4.10}$$

The velocity the charge carriers are travelling at is

$$v = \frac{I}{pAq} \tag{4.11}$$

Where p is the hole concentration, A is the cross-sectionial area of the sample and q is the elementary charge. Combining this with the Lorentz force we get

$$\vec{F} = \frac{IB}{pA} \tag{4.12}$$

Since the force from an electric field is $\vec{F} = q\epsilon$ we can write

$$\epsilon = \frac{IB}{qpA} \tag{4.13}$$

Finally, the magnitude of the Hall voltage is the electric field multiplied by the width of the sample

$$V_H = w\epsilon = \frac{wIB}{qpA} \tag{4.14}$$

The width of the sample is $2r$ and the cross-sectional area is $2rt$ where t is the thickness of the sample. From that we get

$$V_H = \frac{IB}{qpt} \tag{4.15}$$

The sheet density p_s is defined as the density of holes multiplied with the thickness of the sample. We can further write

$$V_H = \frac{IB}{qp_s} \tag{4.16}$$

This can be rearranged to find the sheet carrier density

$$p_s = \frac{IB}{q|V_H|} \tag{4.17}$$

The strength of the magnetic field is $B = 0.5\text{T} = 5 \cdot 10^{-5} \frac{wb}{cm^2}$. As with the Van der Pauw measurements, the Hall measurements are also done around the entire sample using all contacts. We do a total of 8 measurements, 4 measurements of each polarity of the magnetic field. The polarity is reversed to eliminate any offsets in the measurement process.

Denotation of Hall voltages

$V_{direction}$**, Negative N or positive P magnetic field direction**

$$V_{24} = V_{24}, P - V_{24}, N$$
$$V_{13} = V_{13}, P - V_{13}, N$$
$$V_{42} = V_{42}, P - V_{42}, N$$
$$V_{31} = V_{31}, P - V_{31}, N$$

The overall Hall voltage is then

$$V_H = \frac{V_{24} + V_{42} + V_{13} + V_{31}}{8} \tag{4.18}$$

The sign of this Hall voltage indicates the type of material the sample is made of. If it is positive the material is p-type, and if it is negative the material is n-type.
The charge carrier concentration can also be calculated from

$$\eta = [q\mu_p\rho]^{-1} \tag{4.19}$$

where q is elementary charge, μ_p is the hole mobility and ρ is the resistivity.

4.3.3 Seebeck-coefficient

The Seebeck-coefficient of a material is a measure of the voltage that arises in the material because of the temperature gradient it is subjected to, see

section 2.2.1. The Seebeck-coefficient is negative for negatively charged carriers (electrons), and positive for positively charged carriers (holes).
For both samples we used a set-up at the Research Park under the BATE-initiative [23]. This set-up can be seen in Figure 4.12. The sample is heated,

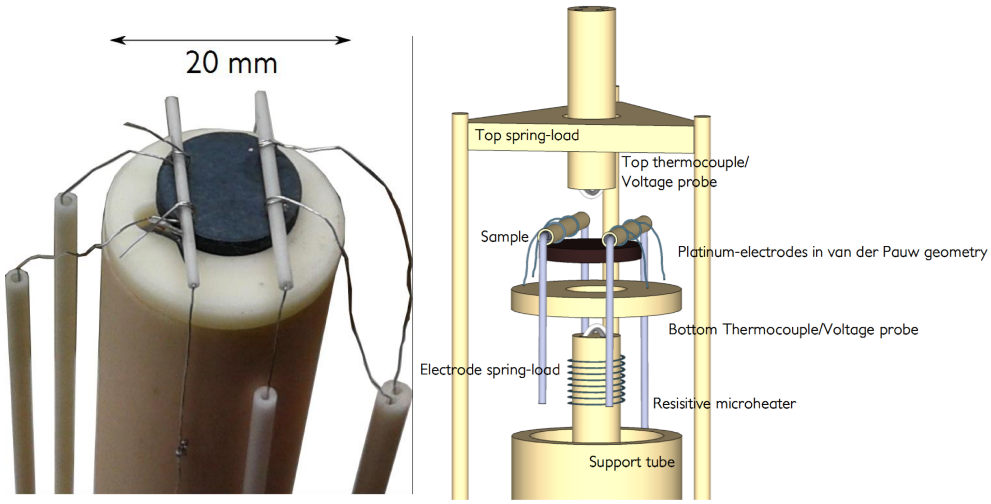

Figure 4.12: High temperature equipment for simultaneous measurement of Seebeck-coefficient and resistivity up to 1200° C, we measured up to 500°.

with a temperature difference between the top and bottom of the sample of around 10°C. The sample is heated from the bottom and the heating is on so that we reach no temperature difference over the sample to ensure that the voltage is zero when the temperature difference is zero. The Seebeck voltage is plotted as a function of the temperature difference across the sample, and the Seebeck-coefficient is determined from the slope of the voltage curve. The measurements where run from 100°C to 500°C.

There is another set-up at the MiNA-lab for determining the Seebeck-coefficient, see Figure 4.13. In this set-up the sample is placed between two copper blocks and the system is protected under a glass bowl. This allows for a measuring of the Seebeck-coefficient under vacuum or with a nitrogen atmosphere. However we did not use this set-up.

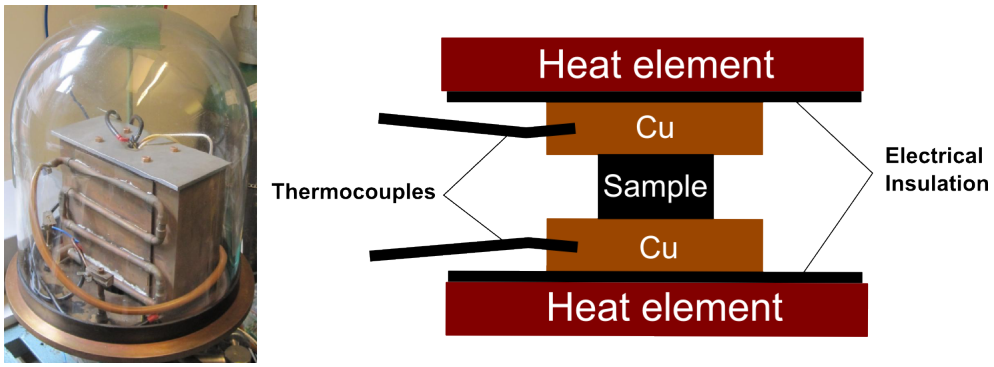

Figure 4.13: Equipment for the measurement of the Seebeck-coefficient. The sample is placed between two copper blocks and thermocouples are attached to each block. The Seebeck voltage is measured through the thermocouples while a constant temperature gradient in the region of 3°C is forced over the sample. The instrument is used at temperatures up to 500°C. [23]

Chapter 5

Results and Discussion

In this chapter we will present the results from the synthesis process and the preparation of samples. We will see what effect the different annealing and sintering temperatures had on phase uniformity and grain sizes.
Further we will look at the characterization of the structure through XRD and SEM analyses and if we managed to make what we wanted to make.
Lastly the results from the electrical characterizations are presented. This includes the thermal conductivity, electrical resistivity, Hall measurements which determines the charge carrier concentrations and mobilities, and the Seebeck measurements.

5.1 Synthesis

The raw materials where melted into ingots in the electric arc-melter at IFE (Figure 4.1). As previously mentioned, samples 1 and 2 where crushed and combined to ensure enough material for sintering and preparations for measurements. As an example these ingots can be seen in Figure 5.1. These ingots has a mass of about 3g each, accurate mass is calculated in Table 4.1.

The samples where crushed in a stamp to obtain powder-form, and also ground more finely with a piston and mortar before annealing. The powders

Figure 5.1: The ingots of samples 1 and 2, named in the text as 'the combined sample'. These ingots where crushed in a stamp and poured together into a pyrex tube for annealing.

where poured into pyrex glass tubes and sealed in vacuum to prevent oxidation.
The combined sample was sintered and annealed at 700°C, while samples 3 and 4 where annealed at 900°C. Sample 3 was also sintered at 900°C.
Sadly, during the annealing, or hopefully during the cooling of sample 4, the glass tube was cracked right at the surface of the powder causing a few milliliters of water to leak in and contaminating the sample. If the crack was there from the start of the annealing process, there is a high risk of oxidation of the powder. If it cracked as it was lowered into the bucket of water for cooling,the sample may still have been usable. We scraped off the powder that seemed darker than the rest, thinking that this part was the only area the water had reached. XRD data will show if there has been significant oxidation. Before sending it to XRD analysis we also kept it in a desiccator for two days for the powder to dry. However we did not go any further with that sample.
We compared XRD-data from the combined sample before and after annealing and saw that many of the secondary phases disappeared or lowered significantly. Still there are some phases that are present in addition to the TiFeSb peaks. Before sintering, sample 3 was again ground in a mortar. This was to break apart large grains that might have formed during annealing and to get finer grain sizes. See Figure 5.2 to see the sample after sintering.

Figure 5.3 shows the combined sample and sample 3 next to each other after they have been prepared for thermal conductivity and Seebeck measurements.

Both samples are solid and are without any visible cracks. The densities are $\rho = 5.8689 \frac{g}{cm^3} (82.78\%)$ and $\rho = 6.5459 \frac{g}{cm^3} (92.33\%)$, with percentage of reference density of $\rho = 7.09 \frac{g}{cm^3}$ [26] in parentheses. A density of around 83% is fairly porous, but at no sign of localized holes, the sample seems good enough for the measurement requirements. Table 5.1 shows the physical measures of the samples after being ground with sand-papers to a size ready for Laser flash and Seebeck measurements.

Figure 5.2: Sample 3 after sintering. The black surface is due to the carbon coating around the sample in the sintering cylinder. The shiny liquid-like substance is the glue used to glue the sample to a metal stub to hold it during the grinding with sand-papers.

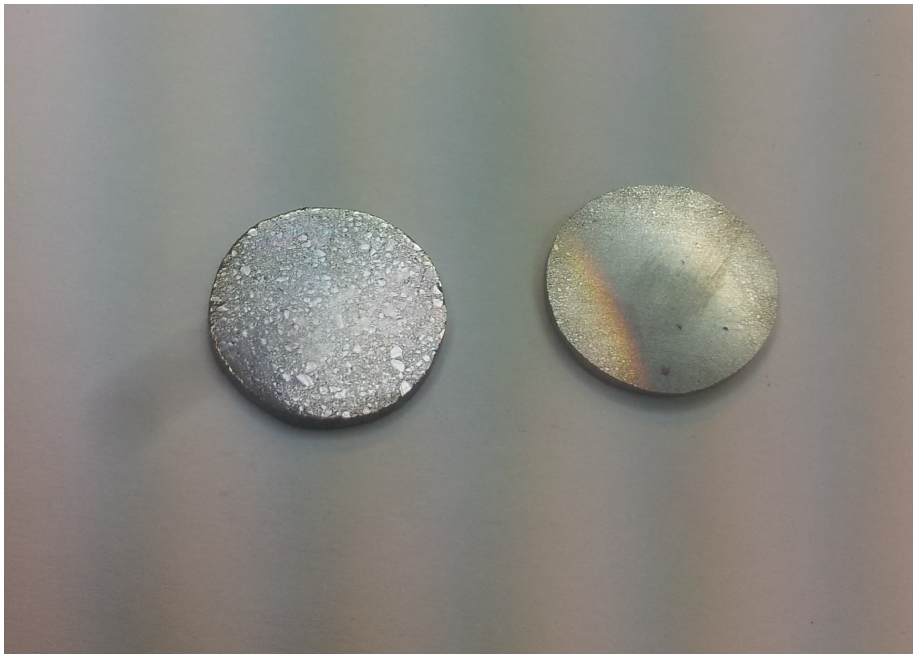

Figure 5.3: The combined sample to the left and sample 3 to the right. One can clearly see the difference in grain sizes.

Table 5.1: Physical Measures

Sample	Diameter[mm]	Thickness[mm]	Mass[g]	Volume [mm^3]	Density [$\frac{g}{cm^3}$]
Combined	12.0	1.76	1.1682	199.05	5.8689
Sample 3	11.9	1.75	1.286	194.64	6.5459

5.2 Structure Characterization

Here we will look at the results from the X-ray Diffraction and pictures from the SEM analysis. The XRD-sample made from the combined sample and the contaminated sample was powder, while for sample 3 we mounted the entire sample on a piece of sticky rubber at the same height the glass plate would have been. A microscopy glass plate was used to push the sample down on the rubber to ensure that it was plane. The SEM analysis consists of pictures of selected areas of the samples and EDS analysis of those areas.

5.2.1 XRD

The X-ray patterns are recorded by a Bruker D8 instrument using CuKα_1 1.54 Å radiation in a Bragg-Brentano geometry. Figure 5.4 shows the X-ray patterns for the combined sample in black, the sample that was contaminated by water in red, and sample 3 in blue. We have marked the Half-Heusler corresponding peaks with the planes they originate from, and marked the Silicon peaks with Si. We also see more peaks present which stems from one or more other phases which we will try to discuss.

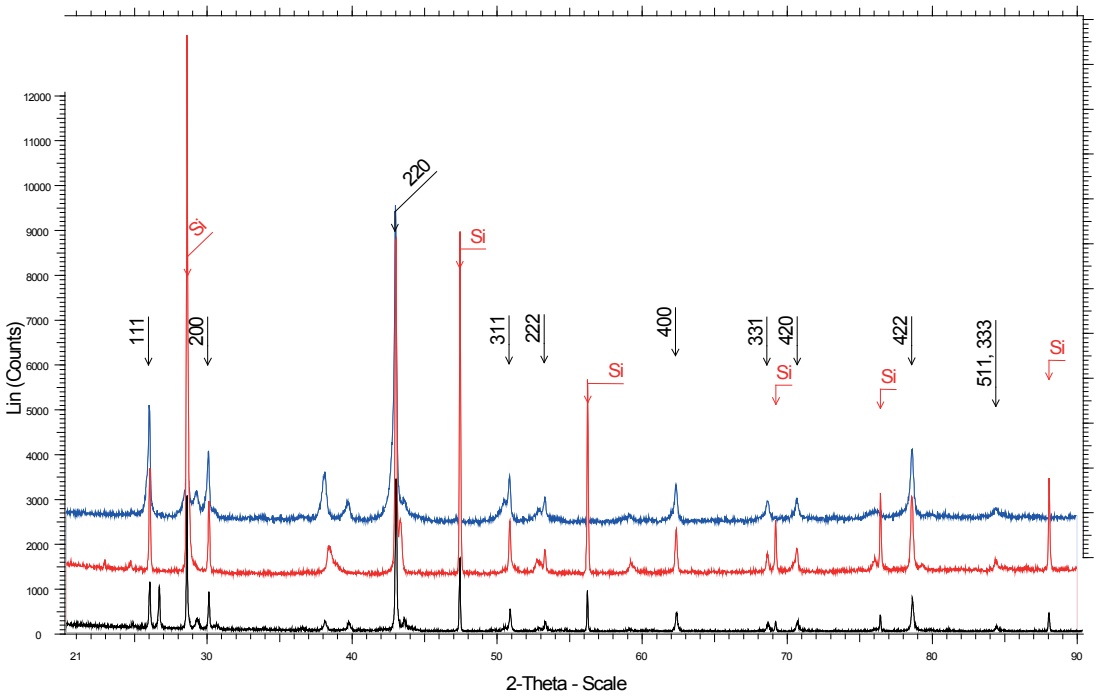

Figure 5.4: X-ray patterns for all 3 samples. The bottom pattern in black is the combined sample, the red one in the middle is the contaminated sample, and the blue one on top is sample 3. Sample 3 was analysed as bulk and did not have a Silicon reference. We notice there are some peaks not corresponding to TiFeSb or Silicon, some alone and other overlapping other peaks. These peaks where very hard to identify.

First of all, the contaminated sample seems to be not as contaminated

as we first assumed. This could be that the powder sent for analysis was not representative of the entire sample, as we scraped away powder that had different colour from the rest.
We will here go through the patterns, giving suggestions based on what we found in available databases and calculated patterns.

Only Silicon was found in the database which corresponded to the peaks in the patterns. The TiFeSb peaks where identified using PowderCell, where we entered the space group and wyckoff-positions, and they fit perfectly. We also used Pearson Crystallographic database with both calculated and experimental patterns to try to identify the phases. The super-cell structure or disordered structure reported from KKR-CPA calculations by [18] could be the cause of the extra peaks, but are not found in the databases. We found a TiFe phase during SEM analysis which is shown in the next section. The peaks from TiFe are in the same place as the TiFeSb peaks so they do not explain the other peaks. Various compositions of TiSb and FeSb and their oxides does not match, neither does any pure Ti, Fe or Sb. Various compositions of TiFeSb where studied, these shifts the peaks a little in different directions and may be the best explanation for the peaks or tails close to the 200, 220, 311 and 222 peaks. There was one oxide of Sb, Sb_2O_4, that could match the peaks at $2\theta = 29.4$ and $2\theta = 30.5$ where other peaks from it disappears due to the low intensity. The same can be said for TiO_3 which had its highest peaks at $2\theta = 38$ and $2\theta = 39.5$. The peak at $2\theta = 26.5$ for the combined sample (black) can be attributed to graphite, where the XRD sample was taken from the edge of the sample after sintering, where some of the graphite used might have been pressed into the sample. This is likely because when the sample is pressed, the edges tend to crack, making room for the graphite to fill the cracks. Sample 3 (blue) shows small peaks at Si locations even though we did not use Si as a reference for this sample. They might come from a few small glass pieces found during SEM analysis shown in the next section. Another reason that some peaks from the suggested phases are visible while others are not, other than having too low intensity, might be of preferred orientation. This also seem unlikely due to a powder

diffraction pattern should have a random distribution of all orientations because it is in powder form, but might apply to the bulk sample. Still there is not much difference between the patterns.

Atleast we can say that the majority of the sample is made from the TiFeSb phase we wanted to achieve.

5.2.2 SEM

Here we will look at selected areas of the samples and suggest the composition of these areas.

The different phases are usually either Titanium and Antimony rich, or Iron rich. Some areas are also found to be either Titanium or Antimony rich, mostly in pits between larger grains. The lighter areas are Titanium and Antimony rich, while the Iron rich areas are darker, in both samples. In sample 3 there where found two small glass pieces which comes from the breaking of the ampoule. These glass pieces had a concentration of a Titanium and Iron phase, nearing $TiFe_2$, around them, and close to no Antimony was found in the same place. The glass might have formed an oxidizing environment around itself which attracted Ti and Fe and repelled Sb. No other interesting areas where found during the SEM analysis. The scale bars on the images had to be added after and are not exact, but can be used as an approximate guide of sizes.
The larger grains which come closest to the 1:1:1 stoichiometry are believed to be the Half-Heusler phases. All phases show the same compositions throughout the sample within 1-3%. If we can average over the two most found phases, the iron rich and the Titanium and Antimony rich phases, we can be tempted to give nominal compositions based on the EDS results. For the combined sample we will give the composition as $Ti_{36}Fe_{30}Sb_{34}$, while for sample 3 the composition would be $Ti_{36}Fe_{29}Sb_{35}$. Based on the error percentages given by the EDS we could also look at compositions being, for the combined sample, $Ti_{36}Fe_{29}Sb_{35}$ or $Ti_{35}Fe_{30}Sb_{35}$, while for sample 3, $Ti_{36}Fe_{28}Sb_{36}$

or $Ti_{38}Fe_{29}Sb_{33}$. Iron is found at low concentrations compared to the other two elements. A reason for this might be that there has been either some unsolved iron in the samples or maybe more tiny glass pieces which iron has formed around during sintering, and then have been grounded away during the sample preparations. These phases of Titanium and Iron around the glass pieces might also be longer in the direction parallel to the view in the SEM, giving a false sense of how big they actually are. Then we will also have to think about where the Antimony went. There could be vast collections of antimony not visible, or also ground away during sample preparations. As is the same for the low Iron concentrations. Then the homogeneity of the samples are questionable.

Another point is that if we look at the oxygen content near the glass piece areas in the last two images, it is around 10% higher than a SiO_2 composition of glass, which might mean that it has created some oxides together with Titanium or Iron, or both.

Images of the combined sample.

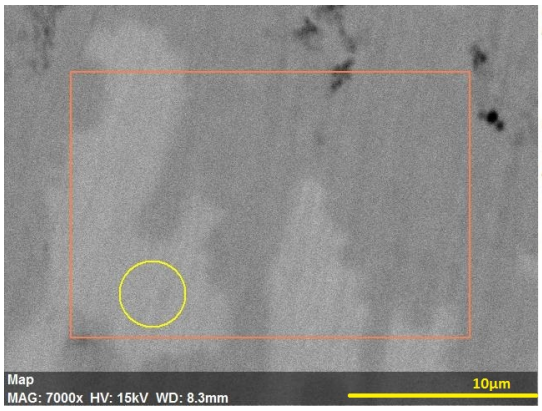

Element	AN	Series	Atom. C [at.%]	Error [%]
Titanium	22	K-series	39.93	0.7
Antimony	51	L-series	37.83	1.7
Iron	26	K-series	22.24	0.5
		Total:	100.00	

(a) Lighter areas are Titanium and Antimony rich.

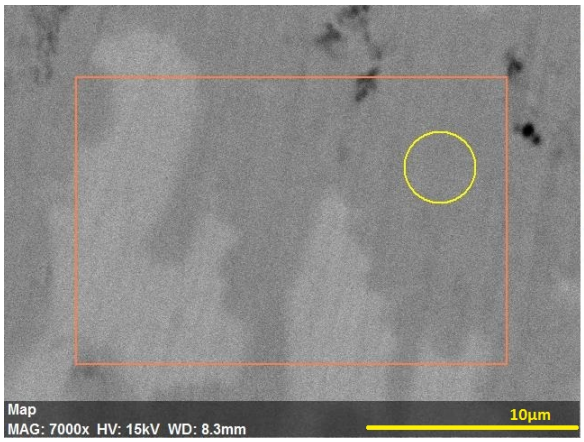

Element	AN	Series	Atom. C [at.%]	Error [%]
Iron	26	K-series	37.99	0.9
Titanium	22	K-series	32.03	0.6
Antimony	51	L-series	29.98	1.5
		Total:	100.00	

(b) Darker areas are Iron rich.

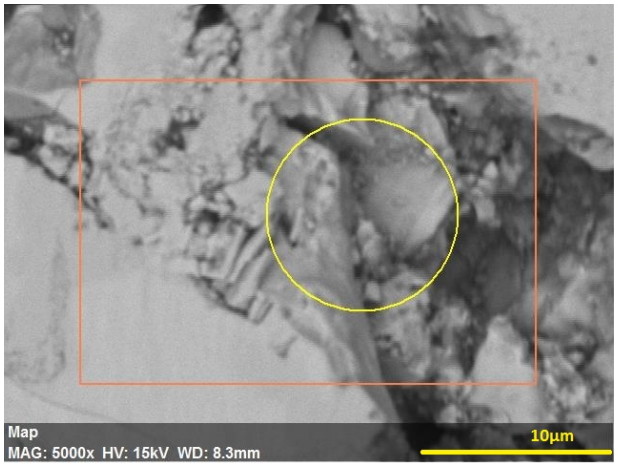

Element	AN	Series	Atom. C [at.%]	Error [%]
Antimony	51	L-series	41.00	2.6
Titanium	22	K-series	33.42	0.8
Iron	26	K-series	25.58	0.8
		Total:	100.00	

(c) Particles between bigger grains. Here Antimony rich.

Images from the combined sample

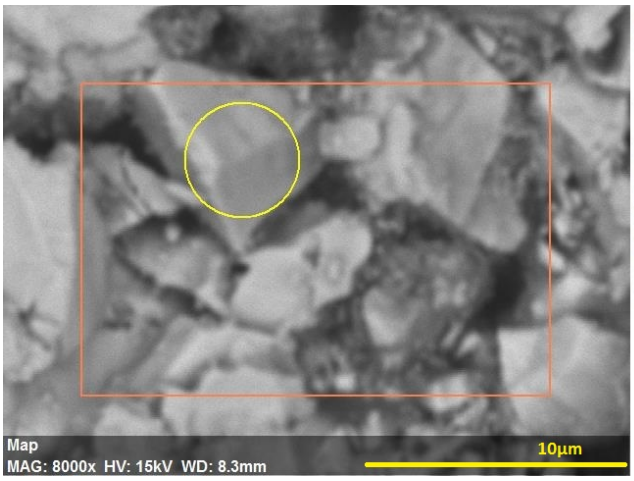

Element	AN	Series	Atom. C [at.%]	Error [%]
Titanium	22	K-series	42.69	0.9
Antimony	51	L-series	39.41	2.1
Iron	26	K-series	17.91	0.5
		Total:	100.00	

(a) Particles between bigger grains. Here Antimony and Titanium rich.

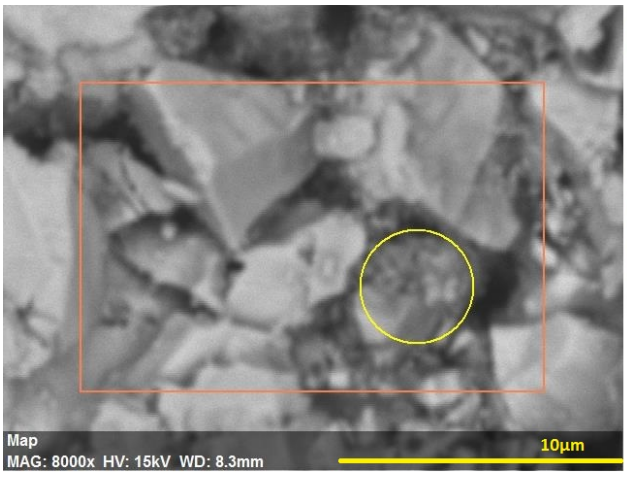

Element	AN	Series	Atom. C [at.%]	Error [%]
Titanium	22	K-series	42.46	0.9
Antimony	51	L-series	28.93	1.5
Iron	26	K-series	28.61	0.7
		Total:	100.00	

(b) Particles between bigger grains. Here Titanium rich.

Images of sample 3.

Element	AN	Series	Atom. C [at.%]	Error [%]
Titanium	22	K-series	40.54	0.7
Antimony	51	L-series	39.12	1.7
Iron	26	K-series	20.34	0.4
		Total:	100.00	

(a) Lighter areas are Titanium and Antimony rich.

Element	AN	Series	Atom. C [at.%]	Error [%]
Iron	26	K-series	37.26	0.9
Titanium	22	K-series	32.42	0.6
Antimony	51	L-series	30.32	1.5
		Total:	100.00	

(b) Darker areas are Iron rich.

Images of sample 3.

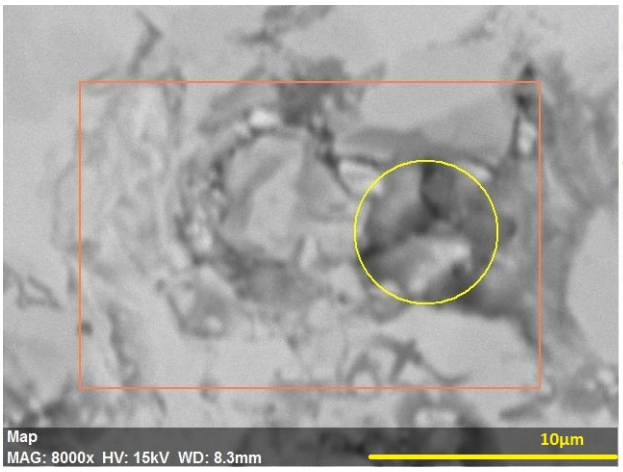

Element	AN	Series	Atom. C [at.%]	Error [%]
Antimony	51	L-series	39.23	2.2
Titanium	22	K-series	37.62	0.8
Iron	26	K-series	23.15	0.6
		Total:	100.00	

(a) Pits between larger grains are usually Antimony and Titanium rich. In this sample the pits also vary between being only Antimony rich and Titanium rich.

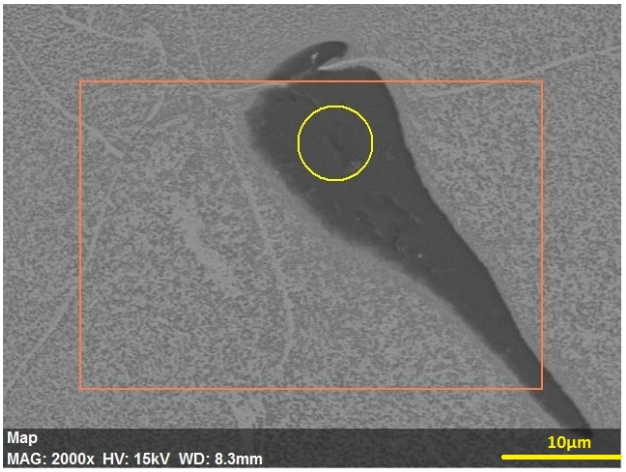

Element	AN	Series	Atom. C [at.%]	Error [%]
Oxygen	8	K-series	64.65	6.3
Silicon	14	K-series	35.35	2.0
		Total:	100.00	

(b) One of the glass pieces found in sample 3 with Titanium and Iron around.

Images of sample 3.

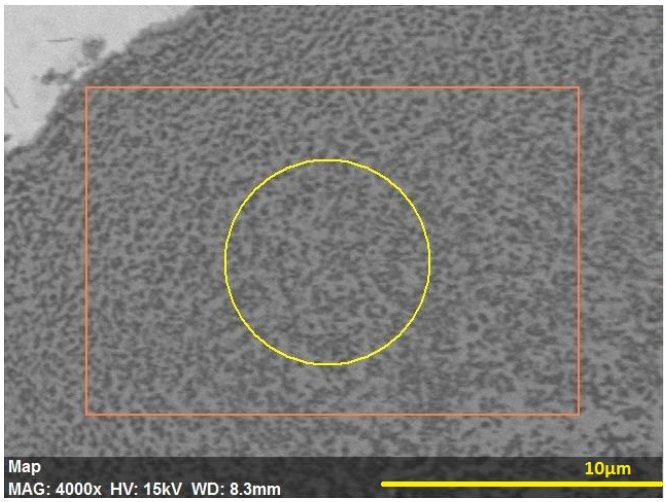

Element	AN	Series	Atom. C [at.%]	Error [%]
Iron	26	K-series	38.63	1.6
Oxygen	8	K-series	30.20	1.8
Titanium	22	K-series	20.27	0.7
Silicon	14	K-series	10.43	0.3
Antimony	51	L-series	0.48	0.1
		Total:	100.00	

(a) Titanium and Iron around the glass piece in figure (b) of the previous set of images. This could also have made oxides of Titanium and Iron.

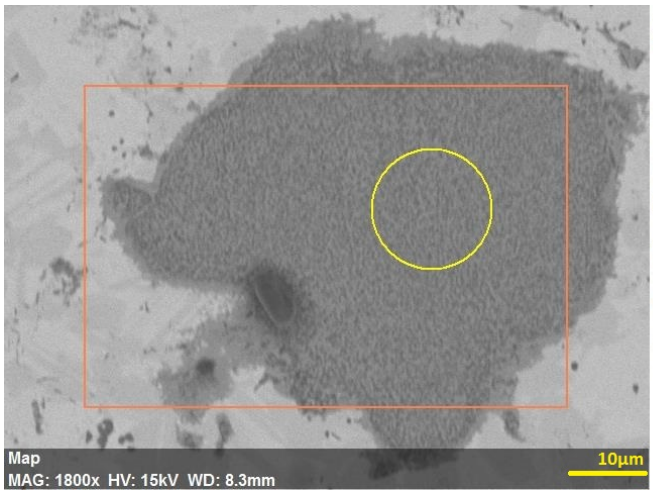

Element	AN	Series	Atom. C [at.%]	Error [%]
Iron	26	K-series	37.89	1.5
Oxygen	8	K-series	31.42	2.1
Titanium	22	K-series	21.28	0.7
Silicon	14	K-series	9.41	0.3
		Total:	100.00	

(b) Titanium and Iron around the other glass piece. A little higher concentration of Titanium around the borders, no Antimony found here.

5.3 Electrical Characterization

Here we present the results from the electrical characterizations, in the order of thermal conductivity, electrical resistivity and Hall measurements, and lastly the Seebeck-coefficient. From these results we can calculate the ZT of the material.

5.3.1 Thermal Conductivity: Laser Flash Measurements

See Figure 5.10 for the measurement of the combined sample. The specific heat of a material shows how much energy is needed to increase the temperature of the material, and is given by $\frac{J}{g \cdot K}$. We see from Figure 5.10 (a) that it needs more energy for higher temperatures except between 200-350°C where it reaches a plateau. It then rises from 350°C.
Thermal Diffusivity is a measure of how fast the heat travels through the sample. A lower diffusivity will then cause a lower thermal conductivity. The combined sample has a diffusivity a little lower than quartz [27]. Since the specific heat rises while the diffusivity lowers, we should see a more flat curve for the thermal conductivity, which we do.
The thermal conductivity is very stable until the sample reaches 350°C because of the competing specific heat and diffusivity, from there they both rise so we see an increase in the thermal conductivity as well. Typically, for semiconductors, the conductivity starts high before lowering and flattening out for higher temperatures. Since it rises at higher temperatures, it confirms the sample to be more metallic. Still it has a lower conductivity than the state of the art p-type materials given in the table on page 34 of the paper of Graf et al. [8], where the best of them, $Zr_{0.5}Hf_{0.5}CoSb_{0.8}Sn_{0.2}$, has a conductivity of 3.6-4.1 W/m·K.

For sample 3, we did not manage to determine the specific heat of the sample. The program used to calculate the different parameters gave the same errors on multiple runs for the pyroceram sample used to calculate the specific heat. We also tried with a silicon sample, but received the same error. Therefore we chose to enter the specific heat values for the combined sample to make

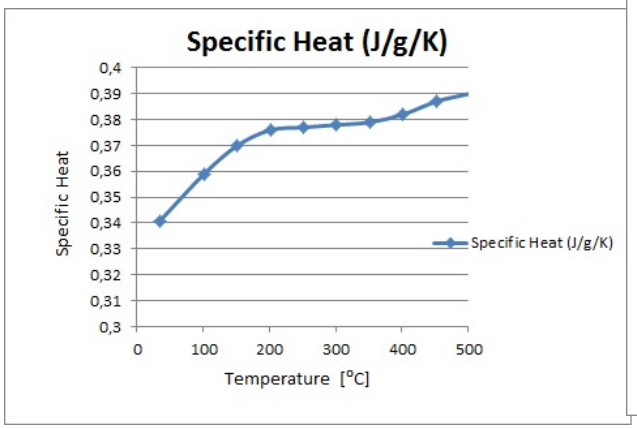

(a) Specific Heat of the combined sample

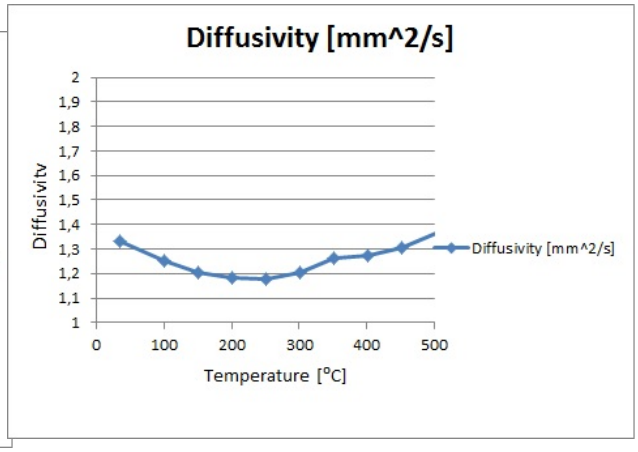

(b) Diffusivity of the combined sample

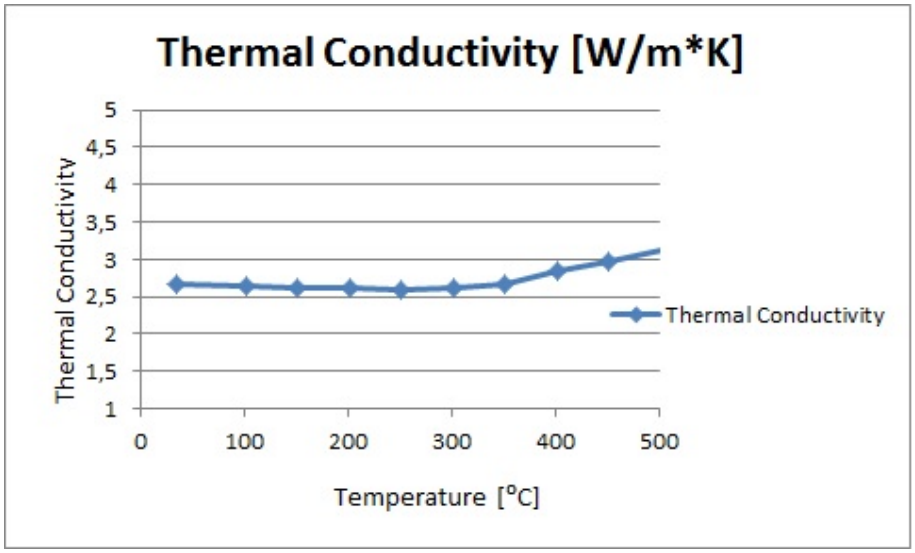

(c) Thermal Conductivity of the combined sample

Figure 5.10: Laser Flash measurement of the combined sample: (a) Specific Heat: We see the sharpest rise at the lower temperatures before a plateau at 200°C, from 350°C it rises again, but not as much as for lower temperatures. (b) Diffusivity: About the same for the first and last measurements. At the middle temperatures the values are lower, which means the heat uses a longer time to go through the sample. (c) Thermal Conductivity: Very flat curve until the sample reaches a temperature of 350°C. The fact that the conductivity rises at higher temperatures is usual for metals.

the measurement. This will give us a higher thermal conductivity than it should be since sample 3 is denser than the combined sample, meaning more mass at the same volume. This leads to sample 3 having an expected specific heat lower than the combined sample. The measurement uses an energy of up to 18 J/pulse for the laser pulses [28]. So from the formula for specific heat, we can get a sense of how much the thermal conductivity is off by a rough calculation. Mass taken from Table 5.1, where we calculated the mass of sample 3 by its density times the volume of the combined sample for constant volume and with a temperature rise of 50 K

$$C_p = \frac{Q}{m\Delta T} \tag{5.1}$$

$$C_{p,combined} = \frac{18J}{1.1682g \cdot 50K} = 0.308 \tag{5.2}$$

$$C_{p,sample3} = \frac{18J}{1.303g \cdot 50K} = 0.276 \tag{5.3}$$

$$\text{Difference} = 1 - \frac{0.308}{0.276} = 10.4\% \tag{5.4}$$

We can see that it is around 10% off. The value for C_p for the combined sample also changes with temperature as can be seen from the measurement, and we see that the calculated value is lower than what was measured, but as said this was only a rough calculation to get a sense of how different they can be. The Laser Flash system uses the pyroceram sample mounted in a holder next to our sample to calculate the specific heat. This sample has a known specific heat and is run parallel at the same time for the same temperatures. Based on what is measured for that sample, specific heats can be calculated. Figure 5.11 will show the results for sample 3. The thermal conductivity is significantly higher in this sample compared to the combined sample, even with a 10% correction. A reason could be that the sample is more dense or that the phonon scattering is less. The diffusivity is also higher, giving a higher conductivity. This thermal conductivity is in the range of the state of the art $Zr_{0.5}Hf_{0.5}CoSb_{0.8}Sn_{0.2}$, shown in the Graf et al. paper, of 3.6-4.1 W/m·K.

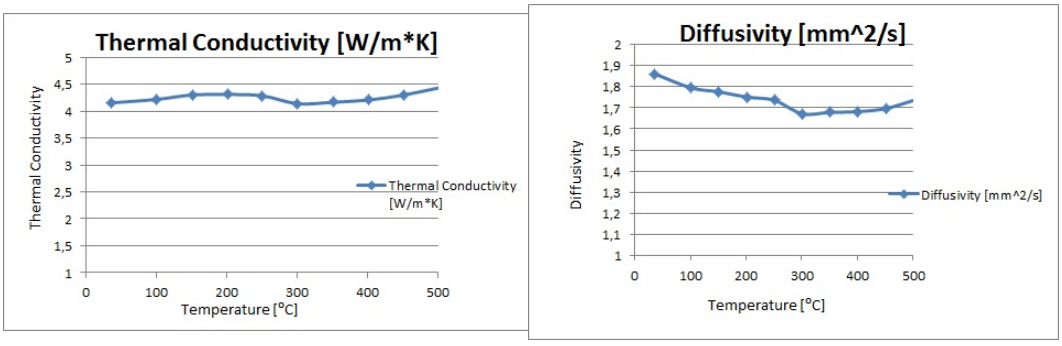

(a) (b)

Figure 5.11: Thermal conductivity and diffusivity of sample 3: Figure (a) shows the thermal conductivity and figure (b) shows the diffusivity. These values are around 10% wrong because of the specific heat used where the same as for the combined sample. This sample also has a fairly flat thermal conductivity curve, and we see the same rise beginning at 350°C as for the combined sample. The diffusivity is higher compared to the combined sample, and the thermal conductivity is also higher even if we adjust for the 10%. Here the diffusivity does not rise up to the value it started out with, as it did for the combined sample.

Table 5.2 shows the electronic thermal conductivity based on the equation

$$\frac{\kappa_e}{\sigma} = LT \tag{5.5}$$

for the lowest and highest temperatures.

Table 5.2: Electronic contribution to Thermal Conductivity (W/m·K)

Temperature [°C]	Combined sample	Sample 3
50	0.387	0.440
450	0.895	1.280

Based on these numbers we see that there actually is a fair contribution from the electrical thermal conductivity when compared to the measured total thermal conductivity, much because of the high electrical conductivity shown in the next section.

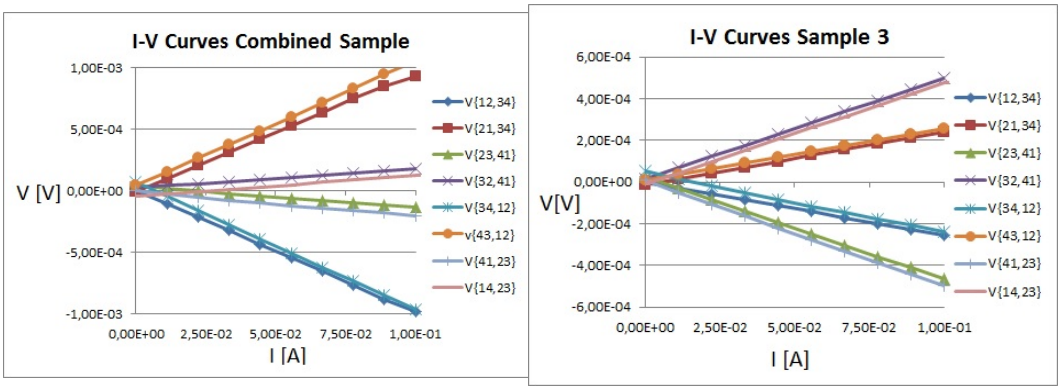

(a) (b)

Figure 5.12: I-V Curves for both samples. Figure (a) shows I-V curves for the combined sample while figure (b) shows I-V curves for sample 3. Current input ranges from 10^{-6}A - 10^{-1}A. Both samples show a small offset for current directions which should overlap, for example V(12,34) and V(34,12), but they are linear.

5.3.2 Van der Pauw Resistivity and Hall Measurements

The Van der Pauw and Hall measurements are done in the set-up shown in Figure 4.9. We can start off by showing some I-V curves of the samples in Figure 5.12. The I-V curves show a small offset in both current directions, but it is not much. The resistivity values are averaged between these. The resistivity is measured between 50°C to 450°C for both samples, and measurements are done around the sample through all contact points, with both current directions and averaged out to obtain a more precise value of the resistivities. The current input starts at 10^{-6}A then jumps to 10^{-3}A and does steps of 10 mA up to 100 mA.

Before the measurements, the combined sample was ground down to a thickness of 0.8 mm, while sample 3 had a thickness of 1.05 mm.

The I-V curves show a small offset between lines who should lie on top of each other, but this difference is very small. At increasing temperatures the curves does not cross the point of zero voltage at zero current. This is most

likely from thermoelectric effects. When current is sent through the sample, the Peltier effect can have an impact on the heat in the sample, where it will cause one side of the sample to warm up and the other side to cool down. The Seebeck effect will cause a current in the sample if the heating causes a difference in the temperature over the sample, depending on how the sample is heated by the element for measurements at different temperatures. Both effects can strengthen each other in that the Peltier effect causes a thermal gradient for the Seebeck effect, and then the Seebeck effect causes a current for the Peltier effect. But these effects also reverse when the input current is reversed, so the effects are practically minimized because of the use of both polarities.

Sample 3 shows a lower resistivity than the combined sample. The resistivity of the combined sample is approximately constant for all temperatures, while sample 3 shows a semiconductor like behaviour with a reducing resistivity for higher temperatures.
A note on why we measure resistivity and not resistance; resistivity is an intrinsic property of a material. This means that the resistivity is constant even if the shape or size of the material is changed. The resistance of a material changes when these parameters are changed. A thin and long sample would show a higher resistance than a short and thick sample. Also, the electrical conductance can be found by taking the inverse of the resistivity.

From quantum mechanics we know that electrons can only occupy certain fixed energy levels. The collection of many levels close together are called energy bands. The most important bands for electrical conductivity are the valence band and the conduction band. The border between these bands is called the fermi level. If the fermi level of the material is at the valence band maximum, the material is p-type, while for n-type materials the fermi level is at the conduction band minimum. The difference in energy between these bands is the band gap. For metals the fermi level is inside a band giving rise to free conduction electrons, while in semiconductors the electrons needs to be excited by external energy to jump from the valence band to the conduc-

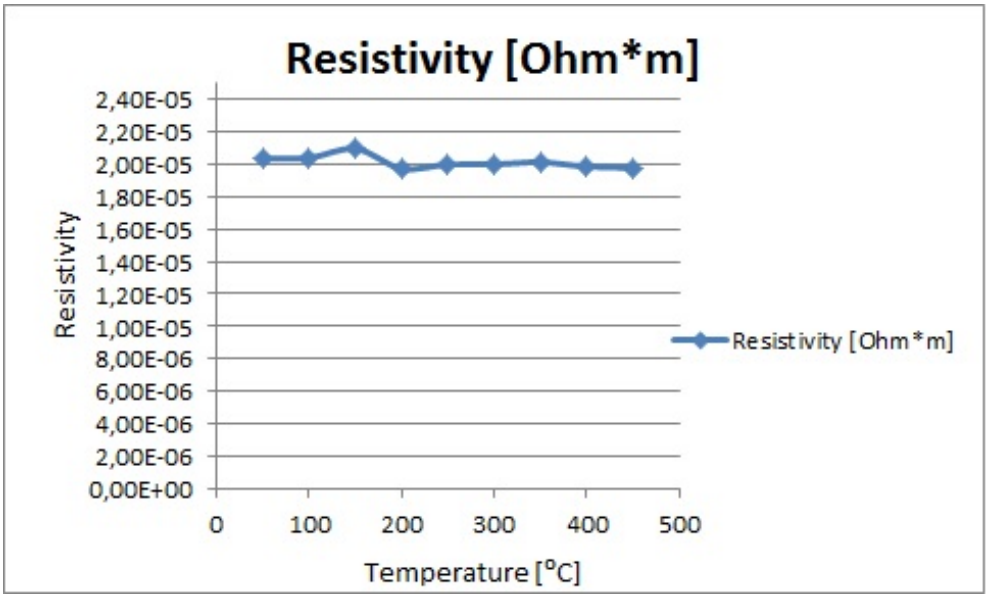

(a)

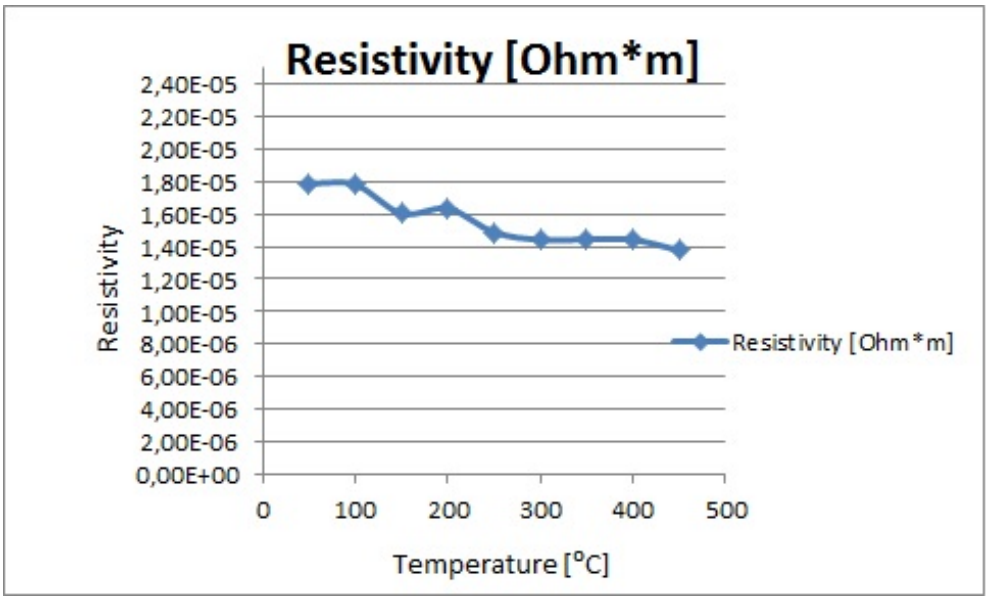

(b)

Figure 5.13: Resistivities: Figure (a) shows the resistivity of the combined sample, while Figure (b) shows the resistivity of sample 3. A more constant resistivity for all temperatures can be seen for the combined sample compared to sample 3. Sample 3 shows here a more semiconductor like behaviour of the resistivity where it reduces at higher temperatures. The same cannot be said for the combined sample.

tion band allowing them to conduct electricity. The main external energy at lower temperatures is heat, they are thermally excited. This is why the resistivity reduces at higher temperature. From Figure 3.5 we see that the fermi level is at, or even inside, the valence band, predicting the material to be p-type. We see the highest density of states near the fermi level, further predicting the material to be a good conductor with low resistivity. This is shown by the measurements.

Figure 5.14 will show the mobilities and the charge carrier concentrations of the two samples. The majority charge carriers in our material are holes because it is p-type. The mobility is a measure of how easy the charge carriers can move in the material, while the carrier concentration is how many charge carriers are in a given volume. They are linked together with the resistivity according to equation 4.19, and are inversely proportional to each other.

The combined sample has a higher average mobility, and then a lower average carrier concentration, than sample 3. Both samples have a drastic increase in mobility at respective temperatures 150°C and 100°C. They both start with a mobility a little over zero, then rises to around 200 $\frac{cm^2}{Vs}$ before reducing for higher temperatures. The mobility is reduced most likely because of increased collisions with phonons as the temperature rises. Sample 3 is more constant after the reduction than the combined sample. The carrier concentration can be explained by the mobility. If the carriers hardly move around, the concentration of carriers in a given area is higher than if they have a higher mobility. Both samples have carrier concentrations in a range corresponding to the border between semimetals and metals [29]. The combined sample is mostly in the 10^{21} range, while sample 3 is more in the 10^{22} range. Table 5.3 will shows the carrier concentrations and mobilities.

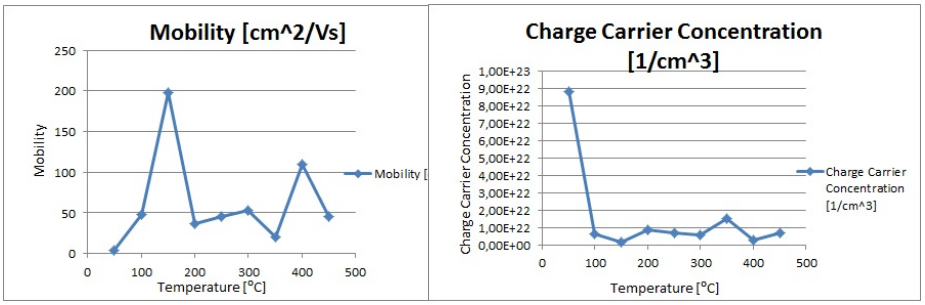

(a) (b)

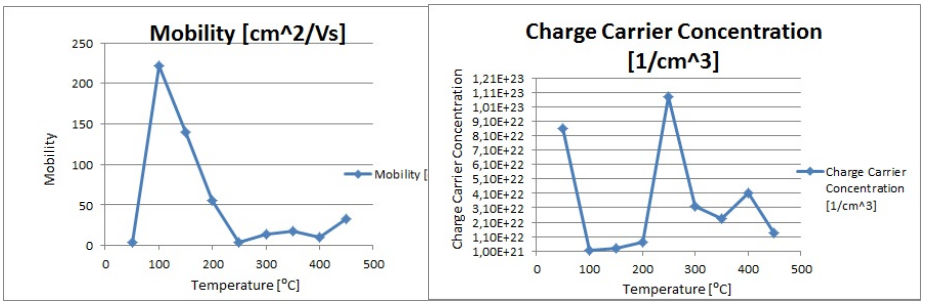

(c) (d)

Figure 5.14: Mobility and Charge Carrier Concentration of both samples. Figure (a) shows the mobility of the combined sample, (b) Carrier Concentration of the combined sample, (c) Mobility of sample 3 and (d) Carrier Concentration of sample 3.

Table 5.3: Carrier Concentration [1/cm^3] and Mobilities [cm^2/Vs]

Temperature [° C]	50	100	150	200	250	300	350	400	450
Combined sample									
Carrier Concentration	$8.84{\cdot}10^{22}$	$6.39{\cdot}10^{21}$	$1.5\cdot10^{21}$	$8.59{\cdot}10^{21}$	$6.96{\cdot}10^{21}$	$5.88{\cdot}10^{21}$	$1.51{\cdot}10^{21}$	$2.88{\cdot}10^{21}$	$6.98{\cdot}10^{21}$
Mobility	3.47	47.91	198.48	36.79	44.84	53.10	20.51	109.08	45.15
Sample 3									
Carrier Concentration	$8.58{\cdot}10^{22}$	$1.58{\cdot}10^{21}$	$2.78{\cdot}10^{21}$	$6.95{\cdot}10^{21}$	$1.08{\cdot}10^{23}$	$3.23{\cdot}10^{22}$	$2.38{\cdot}10^{22}$	$4.13{\cdot}10^{22}$	$1.39{\cdot}10^{22}$
Mobility	4.07	221.76	139.94	54.96	3.89	13.39	18.18	10.48	32.64

From the Hall measurements we measured a positive Hall voltage for both samples, further confirming the samples to be p-type. From equation 4.15 we can show that for the combined sample we have $V_H = 4.41 \cdot 10^{-7}$V(50°C) and $V_H = 5.59 \cdot 10^{-6}$V(450°C), and for sample 3 we have $V_H = 3.47 \cdot 10^{-7}$V(50°C) and $V_H = 2.14 \cdot 10^{-6}$V(450°C).

5.3.3 Seebeck-coefficient

Here we will see the Seebeck-coefficients of the samples in Figure 5.15. The measurements are run from 100°C to 500°C in the set-up shown in Figure 4.12. These Seebeck-coefficients are around 10 times lower than that of Si found in a table of ref. [30], but these values are prone to variation as it depends on the quality and doping of the materials. It is also significantly lower than the coefficients found for the $FeV_{(1-x)}Ti_xSb$ made by Zou et. al in ref. [7], by 2-3 times.

We see that the maximum of the Seebeck-coefficients lie in the temperature range of 200°C to 400°C for both samples. It is assumed that the coefficients for the combined sample will keep reducing at higher temperatures which is more clearly seen for sample 3. The Seebeck effect is dependent on the ability of the material to maintain an as large as possible voltage difference across the sample because of the net build up of charge on one side of the sample. If the charges move easily through the sample, the build up of charges will not be as high, resulting in lower Seebeck-coefficients. This can be optimized by reducing both charge carrier concentration into the range proposed by Yang

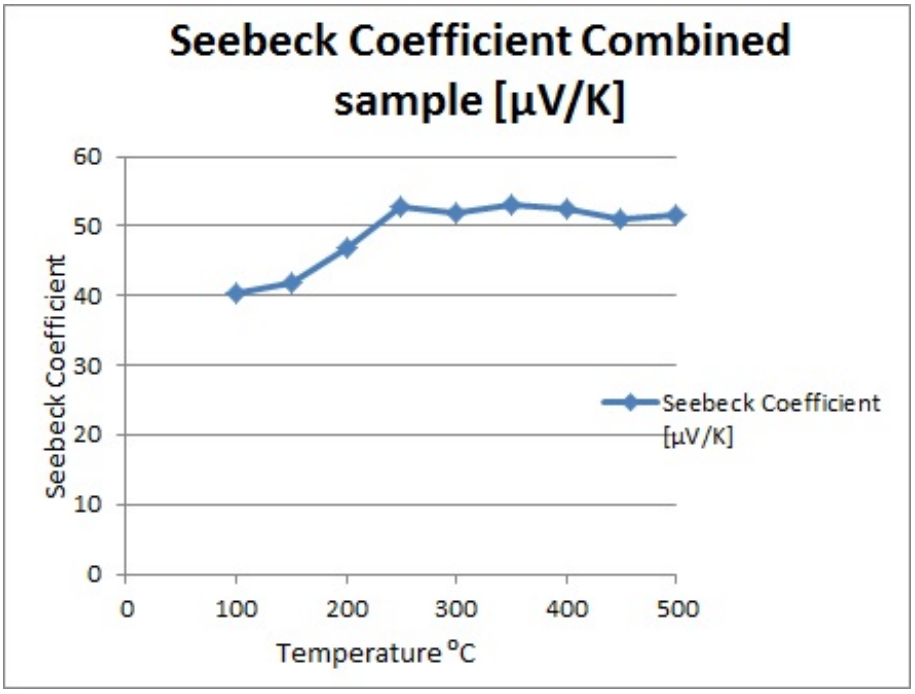

(a)

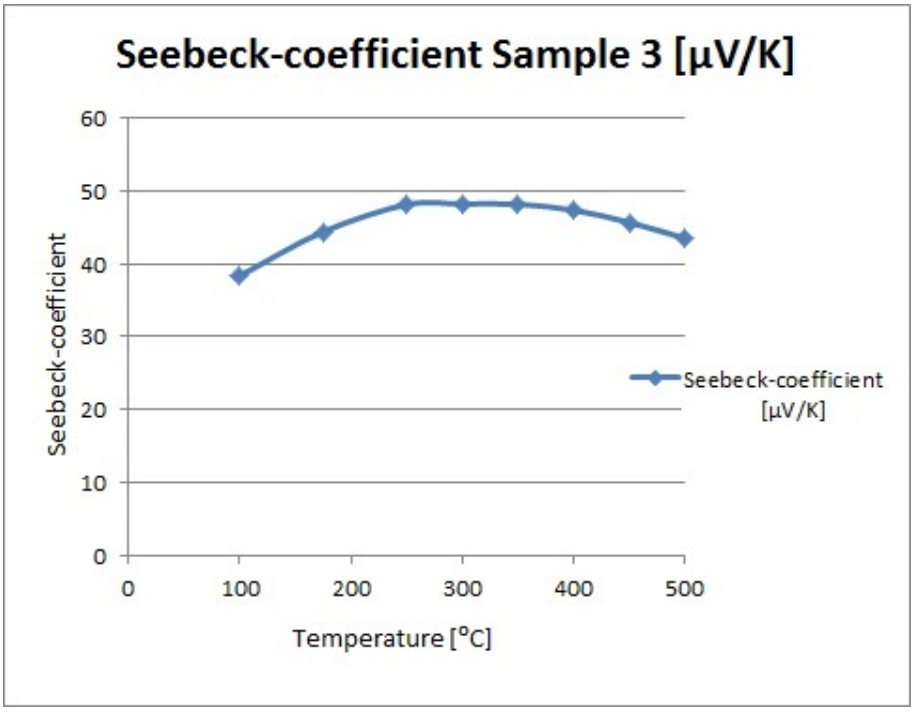

(b)

Figure 5.15: Seebeck coefficients of both samples. Figure (a) shows the Seebeck-coefficients for the combined sample, while Figure (b) shows the Seebeck-coefficients of sample 3. The combined sample shows the highest Seebeck-coefficients.

et. al in ref. [16], and electrical conductivity.

5.3.4 ZT

Here we will give the calculated ZT values for the samples in a temperature range of 100°C to 450°C based on the measurements, by equation 2.9. For sample 3 the ZT might be lower than it should be because of the thermal conductivity measurement with the specific heat used. Sample 3 showed both higher thermal conductivity and lower Seebeck-coefficients than the combined sample, while the electrical conductivity is lower, but the ZT is still assumed to be lower than for the combined sample. Figure 5.16 will show the ZT of the samples, with numerical values in Table 5.4.

The ZT is measure of how efficient a material is as a thermoelectric material, explained in section 2.3.

The combined sample is shown to have a ZT of around 40% higher than sample 3. Much of this is because of the higher thermal conductivity and the lesser Seebeck-coefficients. The ZT is many times lower than those of the State of the art materials shown in Figure 3.3. Since the Seebeck-coefficients are a square term in the calculation of ZT, we can say that this is the factor that needs most improvement. The thermal conductivities are comparable to the State of the art materials, and the electrical conductivity is high.

Table 5.4: ZT

Temperature [°C]	100	150	200	250	300	350	400	450
ZT								
Combined sample	0.0112	0.0135	0.0200	0.0280	0.0293	0.0328	0.0326	0.0319
Sample 3	0.0073	0.0121	0.0155	0.0190	0.0223	0.0232	0.0231	0.0231

The maximum ZT for both samples are at 350°C, with the combined sample reaching ZT = 0.0328 and sample 3 reaching ZT = 0.0232.

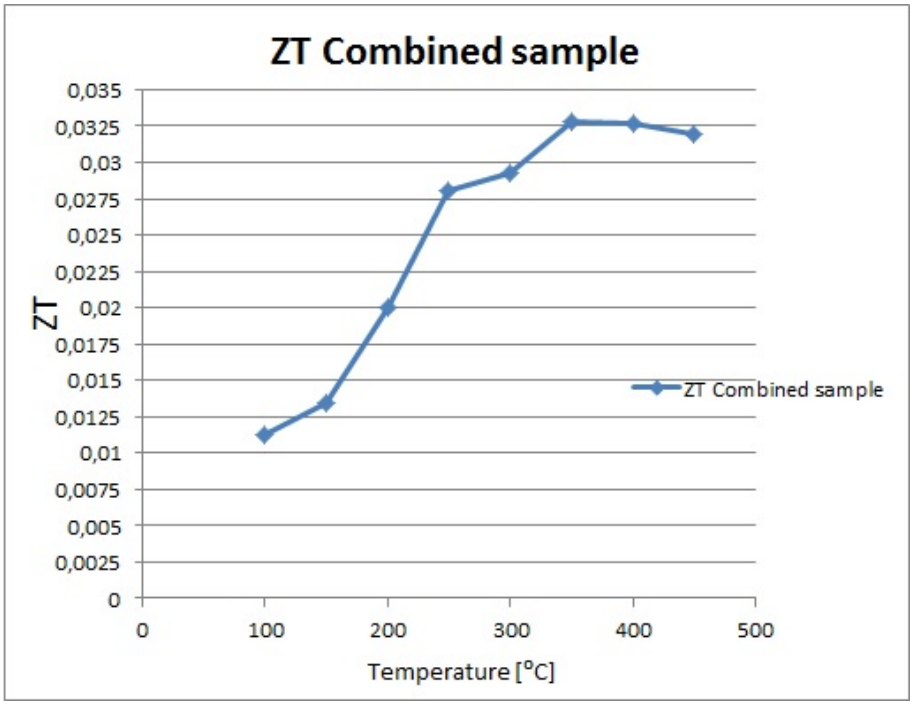

(a)

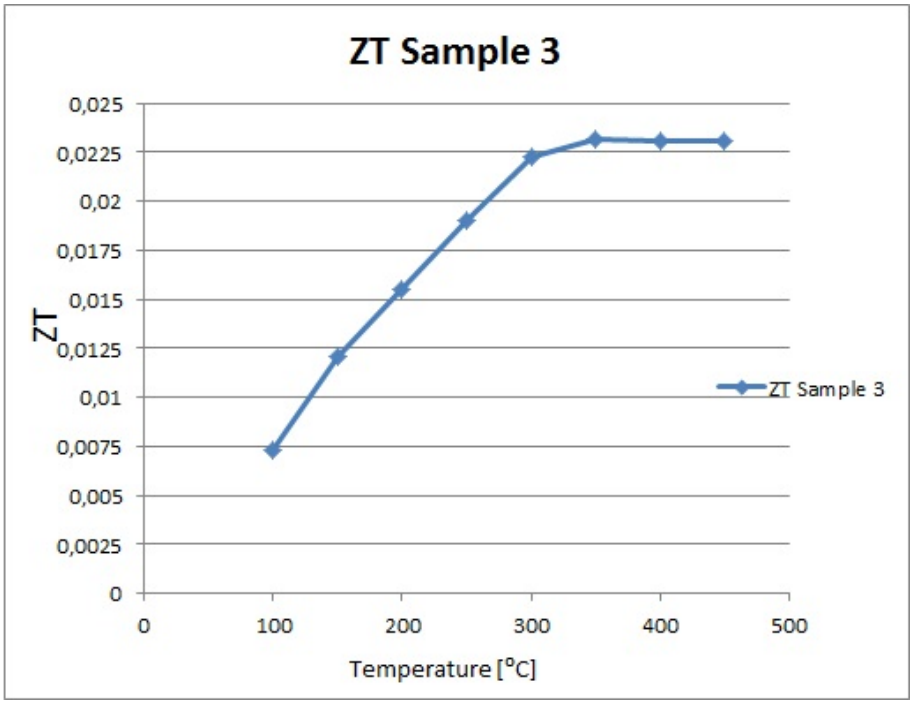

(b)

Figure 5.16: ZT of the samples. Figure (a) shows the ZT for the combined sample, while Figure (b) shows the ZT for sample 3. Highest values for both sample is found at 350°C.

Chapter 6

Conclusion

The objective of this thesis was to synthesize the thermoelectric Half-Heusler alloy TiFeSb, and prepare samples for which thermoelectric properties can be measured.

The experimental work includes synthesis by electric arc-melting, annealing and sintering at different temperatures for phase purity and manipulatable samples. The combined sample was annealed and sintered at 700°C, and sample 3 was annealed and sintered at 900°C. Structural characterization are done by XRD and SEM. Electrical characterizations where done to determine the thermoelectric properties of the samples. We have calculated the ZT of the samples to show their efficiency as a thermoelectric material.

The samples are prepared as disk samples of diameter around 12 mm and a thickness of 1-2 mm depending on different measurements.

Structure characterizations by XRD and SEM where carried out and showed that most of the samples contained the desired phase, with some other phases or structural disorder, and local variations of composition.

Electrical characterization consisted of measurements of Thermal Conductivity, Electrical Resistivity, and Seebeck-coefficients. Also Hall measurements

to determine the type of material.

Thermal Conductivity was carried out in a Laser Flash system between 50°C to 500°C. Electrical Resistivity and Hall measurements where done in a Van der Pauw set-up with silver epoxy for helping the placement of the contacts, in a temperature range of 50°C to 450°C. Seebeck-coefficients where measured in a custom set-up from 100°C to 500°C.

The combined sample showed lesser density and larger grain-sizes compared to sample 3 after synthesis. Both samples show a similarity of phases. They are solid and sample preparation for measurements where of little difficulty. Based on measurements, the samples show a more metallic nature compared to semiconductor behaviour.

The Thermal Conductivity is 30-40% lower for the combined sample compared to sample 3. Respectively the values are in the range of 2.5-3 $\frac{W}{m \cdot K}$ and 4-4.5$\frac{W}{m \cdot K}$. The thermal conductivity for sample 3 needs adjustment as the specific heat was not accurately determined. Both samples have a thermal conductivity comparable with some of the State of the art Half-Heusler materials, and reaches a minimum at 250°C to 350°C. Calculations also show that while phonons are assumed to be the main contributor to the thermal conductivity, the electronic contribution cannot be neglected. The measurements show the samples to be more metallic in nature.

The electrical resistivities show a more semiconductor behaviour for sample 3 compared to the combined sample. The combined sample has a higher resistivity of around $2.0 \cdot 10^{-5}$ Ωm, than sample 3 which had a resistivity of 1.4-1.8$\cdot 10^{-5}$ Ωm, decreasing at higher temperatures.
Mobility and Charge carrier concentration measurements in the Hall set-up shows a higher average mobility and lower carrier concentrations in the combined sample compared to sample 3. The carrier concentration for the combined sample is in range of 10^{21}, while sample 3 is in the range of 10^{22}. The positive sign of the Hall voltages confirms both samples to be p-type.

The Seebeck-coefficients are low compared to State of the art materials, mostly due to the metallic nature of the samples and high carrier concentrations. Both the combined sample and sample 3 show a maximum Seebeck-coefficient at a little over and under 50 $\frac{\mu V}{K}$, respectively.

The calculated ZT for both samples show low values in the range from 0.01 to a little over 0.03. Both reached their maximum ZT at 350°C with ZT = 0.0328 for the combined sample and ZT = 0.0232 for sample 3. The ZT calculations are from temperatures of 100°C to 450°C which where the temperatures in common for all measurements.

Chapter 7

Future work

Based on the work in this thesis we will suggest that the synthesis process is studied more carefully to understand why certain phases form, and more annealing and sintering temperatures should be investigated for phase purity. It is not certain that higher temperatures will help in case certain phases form more easily at higher temperatures and that the different elements diffuse differently. The possibility of a super-structure or disordered structure needs to be investigated.

Work should be done to suggest dopants or substitution elements to manipulate the charge carrier concentrations into a more preferred range, and to increase the Seebeck-coefficients. Doping and substitution will also introduce impurities and disorder to further reduce the thermal conductivity. Sample 3 shows an interesting behaviour of resistivity at increasing temperatures, in that it reduces in a semiconductor way at higher temperatures. It should be investigated why sample 3 shows this trend while the other sample does not.

Further treatment of the samples by, for example, ball-milling for reduced grain-sizes can be carried out, to see what effect it has on the properties.

Bibliography

[1] S Shafiei and R. A Salim. Non-renewable and renewable energy consumption and CO2 emissions in OECD countries: A comparative analysis. *Energy Policy*, 66:547—-556, 2014.

[2] S Shafiee and E Topal. When will fossil fuel reserves be diminished? *Energy Policy*, 37:181—189, 2009.

[3] J. R Sootsman, D. Y Chung, and M. G Kanatzidis. *Angewandte Chemie International*, 48:8616–8639, 2009.

[4] J-F Li, W. S Liu, L. D Zhao, and M Zhou. *NPG Asia Materials*, 2:152––158, 2010.

[5] F Casper, T Graf, S Chadov, B Balke, and C Felser. Half-Heusler compounds: novel materials for energy and spintronic applications. *Semiconductor Science and Technology*, 27:3–6, 2012.

[6] T.M Tritt. Thermoelectric materials: Principles, Structure, Properties, and Applications. *Encyclopedia of Materials: Science and Technology(Second Edition)*, pages 1–11, 2002.

[7] M Zou, J-F Li, and T Kita. Thermoelectric properties of fine-grained FeVSb Half-Heusler alloys tuned to p-type by substituting Vanadium with Titanium. *Journal of Solid State Chemistry*, 198:125—130, 2013.

[8] T Graf, C Felser, and S.S.P Parkin. Simple rules for the understanding of Heusler compounds. *Progress in Solid State Chemistry*, 39:3–5, 32–38, 2011.

[9] D.M Rowe. *Thermoelectrics Handbook - Macro to Nano*. CRC Press, 2006.

[10] H. Alam and S. Ramakrishna. A review on the enhancement of figure of merit from bulk to nano-thermoelectric materials. *Nano Energy*, 2012.

[11] J Taftø and Ø Prytz. Private communication.

[12] F Heusler. *Verhandlungen der Deutschen Physikalischen Gesellschaft*, 5:219, 1903.

[13] F Heusler, W Starck, and E. Haupt. *Verhandlungen der Deutschen Physikalischen Gesellschaft*, 5:220–223, 1903.

[14] C Felser, G.H Fecher, and B Balke. *Angewandte Chemie International*, 46:668–699, 2007.

[15] J Tobola and J Pierre. Electronic phase diagram of the XTZ (X=Fe, Co, Ni; T=Ti, V, Zr, Nb, Mn; Z=Sn, Sb) semi-Heusler compounds. *Journal of Alloys and Compounds*, 296:243–252, 2000.

[16] J Yang, H Li, T Wu, W Zhang, L Chen, and J Yang. Evaluation of Half-Heusler Compounds as Thermoelectric Materials Based on the Calculated Electrical Transport Properties. *Advanced Functional Materials*, 18:2880–2888, 2008.

[17] J Toboła, L Jodin, P Pecheur, and Scherrer H. Composition-induced metal-semiconductor-metal crossover in half-heusler Fe(1-x)Ni(x)TiSb. *PHYSICAL REVIEW B, 155103*, 64:01–07, 2001.

[18] J Tobola, J Pierre, S Kaprzyk, R. V Skolozdra, and M. A Kouacou. Crossover from semiconductor to magnetic metal in semi-heusler phases as a function of valence electron concentration. *Journal of Physics: Condensed Matter*, 10:1013, 1998.

[19] Yumi Hayashi, Sung-Wng Kim, Yoshisato Kimura, and Yoshinao Mishima. Thermoelectric properties of several p- and n-type half-heusler

compounds and effects of dopants. *Advanced Materials for Energy Conversion II, Proceedings of a Symposium held during the TMS Annual Meeting*, pages 367–374, 2004.

[20] Yu Cui, Xie Hanhiu, Fu Chenguang, Zhu Tiejun, and Xinbing Zhao. High performance Half-Heusler thermoelectric materials with refined grains and nanoscale precipitates. *Journal of Materials Research*, 27:2457–2465, 2012.

[21] Xiao Kai, Zhu Tie-Jun, Yu Cui, Yang Sheng-Hui, and Zhao Xin-Bing. P-type doping of Hf0.6Zr0.4NiSn Half-Heusler thermoelectric materials prepared by levitation melting and spark plasma sintering. *Journal of Materials Research*, 26:1913–1918, 2011.

[22] Anna Sypien. Modern materials prepared with the use of levitation melting method in the magnetic fields, 2009.

[23] Infrastructure at BATE. http://www.mn.uio.no/fysikk/english/research/projects/bate/thermoel 2014.

[24] Dieter K Schroder. *Semiconductor Material and Device Characterization, 3rd ed.* John Wiley And Sons, 2006.

[25] Blair Bonnet. Van der pauw method - hall effect. http://en.wikipedia.org/wiki/File:Van_de_Pauw_Method_-_Hall_Effect.png, 2006.

[26] TiFeSb Crystallographic Data. http://www.springermaterials.com/docs/VSP/datasheet/lpfsd/01007000/LPFSD_1007560.html, 2014.

[27] Jim Wilson. Thermal diffusivity. http://www.electronics-cooling.com/2007/08/thermal-diffusivity, 2007.

[28] NETZSCH. LFA 457 MicroFlash - Laser Flash Apparatus. http://www.netzsch-thermal-analysis.com/en/products-solutions/thermal-diffusivity-conductivity/lfa-457-microflash.html#!tabs/technique, 2014.

[29] Charles Kittel. *Introduction to Solid State Physics*. John Wiley and Sons, 8th ed. edition, 2005.

[30] Clemens J. M. Lasance. The seebeck coefficient. http://www.electronics-cooling.com/2006/11/the-seebeck-coefficient/, 2006.